SANDIA REPORT
SAND2023-10581
Printed September 2023

Sandia National Laboratories

Development of a colinear Second-Harmonic Orthogonal Polarization (SHOP) interferometer for electron areal density measurements in Magnetically Insulated Transmission Lines (MITLs)

Nathan R. Hines, Mark A. Gilmore
Electrical and Computer Engineering Department
The University of New Mexico
Albuquerque, NM 87131
nhines@sandia.gov

Thomas J. Awe, Jens Schwarz, Sonal G. Patel, Derek C. Lamppa, Pablo A. Reyes, Daniel J. Scoglietti, George R. Laity, Darrell J. Armstrong, David E. Bliss, Michael E. Cuneo
Sandia National Laboratories
P.O. Box 5800, MS-1195
Albuquerque, NM 87185-9999

David V. Rose
Voss Scientific
418 Washington St SE
Albuquerque, NM 87185-9999

Prepared by
Sandia National Laboratories
Albuquerque, New Mexico 87185
Livermore, California 94550

Issued by Sandia National Laboratories, operated for the United States Department of Energy by National Technology & Engineering Solutions of Sandia, LLC.

Available to DOE and DOE contractors from

U.S. Department of Energy
Office of Scientific and Technical Information
P.O. Box 62
Oak Ridge, TN 37831

Telephone: (865) 576-8401
Facsimile: (865) 576-5728
E-Mail: reports@osti.gov
Online ordering: http://www.osti.gov/scitech

Available to the public from

U.S. Department of Commerce
National Technical Information Service
5301 Shawnee Road
Alexandria, VA 22312

Telephone: (800) 553-6847
Facsimile: (703) 605-6900
E-Mail: orders@ntis.gov
Online order: https://classic.ntis.gov/help/order-methods

ABSTRACT

Experimental measurements of low density plasmas forming in Magnetically Insulated Transmission Line (MITL) regions are desired to improve our understanding of current loss and power flow. Therefore, a new optical interferometer diagnostic was commissioned via this LDRD project. To measure the expected 10^{13} - $10^{17}\,\mathrm{cm}^{-3}$ electron densities inside the 0.5 - 6 mm Anode-Cathode (A-K) gaps, a colinear SHOP interferometer diagnostic was constructed.

The diagnostic was initially fielded on the University of New Mexico (UNM) Helicon-Cathode (HelCat) plasma device which provided a highly repeatable and well understood plasma source for which the colinear SHOP interferometer's functionality could be verified and measured. Utilizing the highly repeatable plasma source and shot averaging, the interferometer was able to achieve an areal density sensitivity of $1 \times 10^{14}\,\mathrm{cm}^{-2}$. This work at UNM lead to a Review of Scientific Instruments (RSI) publication [20], DOI:10.1063/5.0101687.

After the diagnostic's capability was proven at UNM, the colinear SHOP interferometer was commissioned for use on the Sandia National Laboratories (SNL) Mykonos accelerator. Here, it provided the first temporal areal density measurements of plasma formation in a parallel plate MITL. The diagnostic was able to achieve a single shot (no multi-shot averaging like at UNM) areal density sensitivity of $1 \times 10^{15}\,\mathrm{cm}^{-2}$ along a $\sim 2\,\mathrm{mm}$ probing path length, which provided adequate capability to conduct fundamental physics research of MITL plasma formation. CHICAGO and ALEGRA simulations support the diagnostics experimental findings. More experimental and computational work will continue, likely leading to another publication(s). The smaller scale Mykonos accelerator work has also provided justification that the colinear SHOP interferometer is a capable diagnostic for measuring plasma areal densities in the inner MITL and convolute regions of larger TW-class accelerators like SNL's *Z* machine.

This project was supported by REHEDS LDRD project number 222428.

ACKNOWLEDGMENT

Thanks are due to my mentors who helped facilitate much of the progress in project: Derek Lamppa, Jens Schwarz, Thomas Awe, Sonal Patel, and Mark Gilmore.

I wish to thank Robert Obregon for his tireless efforts to load, unload, and refurbish the Mykonos vacuum chamber between shots; Larry Lucero and the RAMP facility for critical last minute machining of hardware components; as well as Karen DeZetter and Michael Montoya for their absolutely essential work ensuring our safety.

I could not have completed this work without support from the team responsible for Mykonos: Derek Lamppa and Brian Hutsel as machine operators and Joshua Leckbee as facility manager, therefore, thanks are due.

I also thank the optical experts for their assistance in educating me: Daniel Scoglietti for his informative talks and help in the lab; Pablo Reyes for his creative design input and simulations; as well as Darrell Armstrong and Arlee Smith for their helpful input on second-harmonic generation.

Thanks go to David Rose and Derek Lamppa for their work on the CHICAGO and ALEGRA simulations respectively.

And finally, a special thanks from me to Derek Lamppa whose help extended well beyond the science.

CONTENTS

LIST OF FIGURES

LIST OF TABLES

1. INTRODUCTION

This introduction discusses the necessity of continued Power Flow (PF) research and the motivation behind this LDRD project's development of a new diagnostic capability. The colinear Second-Harmonic Orthogonality Polarized (SHOP) interferometer diagnostic (generally termed "Dispersion Interferometer (DI)"), provided the capability to directly measure the large range of plasma densities for continued PF research. The chapter is concluded with a review of the diagnostic's historical evolution.

1.1. Power Flow Research Motivation

Large TW-class accelerators such as Sandia's *Z* machine support a variety of stockpile science experiments [1]. PF specific experiments ([2]–[5]), suggest current loss mechanisms occurring in the vacuum convolute and inner Magnetically Insulated Transmission Line (MITL) regions of these accelerators, see Fig. (1.2), reducing their efficiency. Fully relativistic, Monte Carlo Particle-In-Cell (PIC) and MagnetoHydroDynamic (MHD) simulations [6]–[9] suggest plasmas shunting current across the Anode-Cathode (A-K) gap in the inner MITL are the primary source of this current loss. Fig. (1.3) shows CHICAGO simulation results highlighting electron densities in *Z*'s inner MITLs ranging from 10^{13} - $10^{17}\,\mathrm{cm}^{-3}$.

Mitigation of current loss, as well as developing an apprehension of how it scales to future Next Generation Pulsed Power (NGPP) drivers, requires an improved understanding of the plasmas formed in MITL regions. This LDRD's objective is to develop a diagnostic capable of making the first direct measurement of the expected *Z* machine inner MITL gap electron densities of 10^{13} - $10^{17}\,\mathrm{cm}^3$ over a 1 cm path length. Ideally, the diagnostic system would be: (1) probing the plasma using a VISible (VIS) to Near-InfraRed (NIR) wavelength, as it is physically impossible to focus longer wavelength (like microwave) beams through the typical 0.5 - 6 mm inner MITL A-K gaps; (2) fiber-coupled, to simplify probing access inside the complicated MITL geometry; (3) specifically operated at the 1550 nm wavelength, for more convenience being able to source optical components at the common communications wavelength; (4) vibration isolated, to exclude noise from potential mechanical movements of optical components located close to the load region; and (5) rapidly optically aligned, to prevent delays in shot-day operations. A diagnostic capable of meeting all of these criteria is the colinear SHOP interferometer.

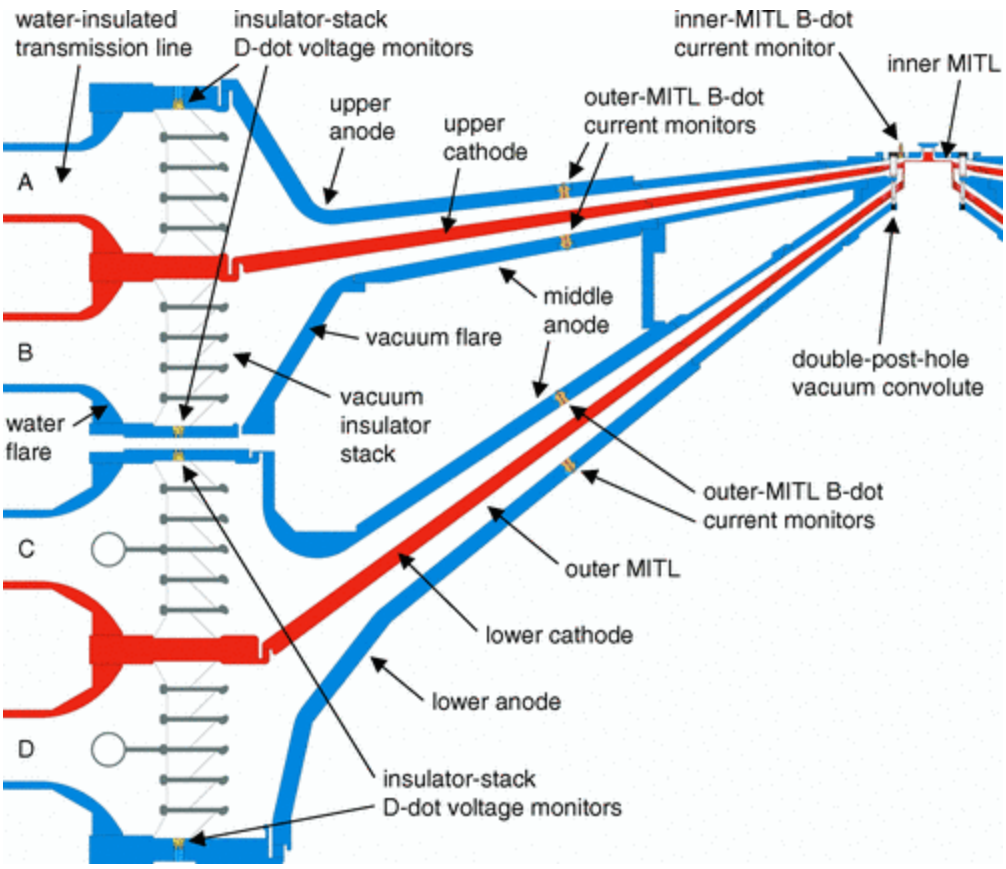

Figure 1.1. Cross-sectional views of Sandia's Z machine outer MITL region [10]. The outer MITL region starts at the insulator-stack, consists of four transmission lines, and ends at the double-post-hole vacuum convolute. Z's outer MITL section is 2.6 m in diameter.

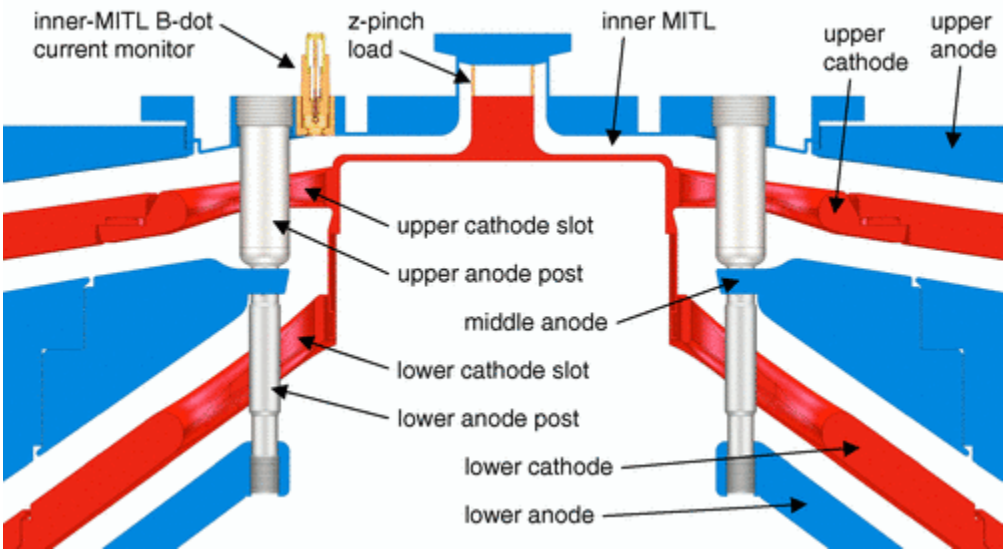

Figure 1.2. Cross-sectional views of Sandia's Z machine double post-hole vacuum convolute and inner MITL region [10]. The double-post-hole vacuum convolute adds the current from the four outer MITLs into a singular inner MITL. The inner MITL spans between the double-post-hole vacuum convolute and load hardware. Z's inner MITL section typically ranges from 12 - 32 cm in diameter.

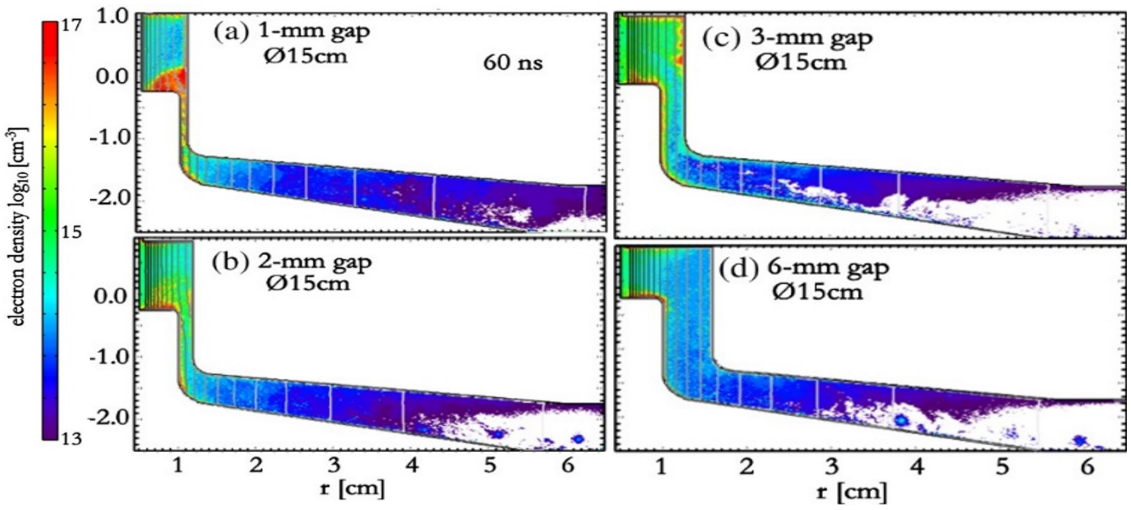

Figure 1.3. 2D CHICAGO PIC electron density simulations of four Z machine inner MITL geometries [8]. The four geometries vary by the A-K gap spacing of their vertical sections, which are (a) a 1 mm gap, (b) a 2 mm gap, (c) a 3 mm gap, (d) a 6 mm gap. These simulations used a 15 cm diameter inner MITL and the results are plotted during the 60 ns time step. Shown are electron densities ranging between 10^{13} - $10^{17}\,\mathrm{cm}^{-3}$.

1.2. Colinear SHOP Interferometer History

The first colinear two-wavelength optical interferometer (the first "dispersion interferometer"), used for plasma density measurements was developed by General Atomic Co. on the Doublet III Tokamak in 1977 [11]. This interferometer utilized two separate laser sources, CO_2 at 10600 nm and HeNe at 633 nm. The first designs published utilizing a single laser source and Second-Harmonic (SH) generation for the second colinear wavelength were by F. Hopf from 1980-1982 [12]–[14]. SH generation via nonlinear crystals is discussed further in Sec. (3.2). The first colinear SH interferometer to include a mutually orthogonal polarization splitting detection scheme (the first "colinear SHOP interferometer") was used on a gas-dynamic trap in 1993 [15]. Conveniently, this mutually orthogonal polarization splitting equally balances the two independent SH intensity fluctuations, allowing for increased refractive index sensitivity. More on this polarization splitting and the relationship between the SHOP interferometer's output signal and correlated areal density is discussed in Sec. (3.3).

Though the colinear SHOP interferometer diagnostic designed throughout this LDRD project is based on the original scheme [15], several necessary changes/improvements were implemented to increase the spatial and temporal resolution without reducing the refractive index detection sensitivity. This allowed the diagnostic to successfully resolve electron areal densities in MITL A-K gaps.

There have been several other colinear SHOP interferometers with varying refractive index sensitivities and time resolutions [16]–[20], compared in Fig. (1.4). Additionally, there have been several 2D versions [21]–[23], though they don't have sufficient temporal resolution for PF applications. The single shot sensitivity of the colinear SHOP interferometer built throughout this LDRD project was $\langle n_e L\rangle \approx 10^{15}\,\mathrm{cm}^{-2}$. The sensitivity limit is due to the system's obtainable signal-to-noise ratio, shown in Fig. (1.5). The sensitivity was lowered to $\langle n_e L\rangle \approx 10^{14}\,\mathrm{cm}^{-2}$ when

utilizing multi-shot averaging to reduce noise [20]. Though there is an opportunity for signal-to-noise ratio improvement on the diagnostic, we do not presently known how to obtain a $\langle n_e L \rangle = 10^{13}\,\mathrm{cm}^{-2}$ areal density sensitivity with a 1 ns temporal resolution.

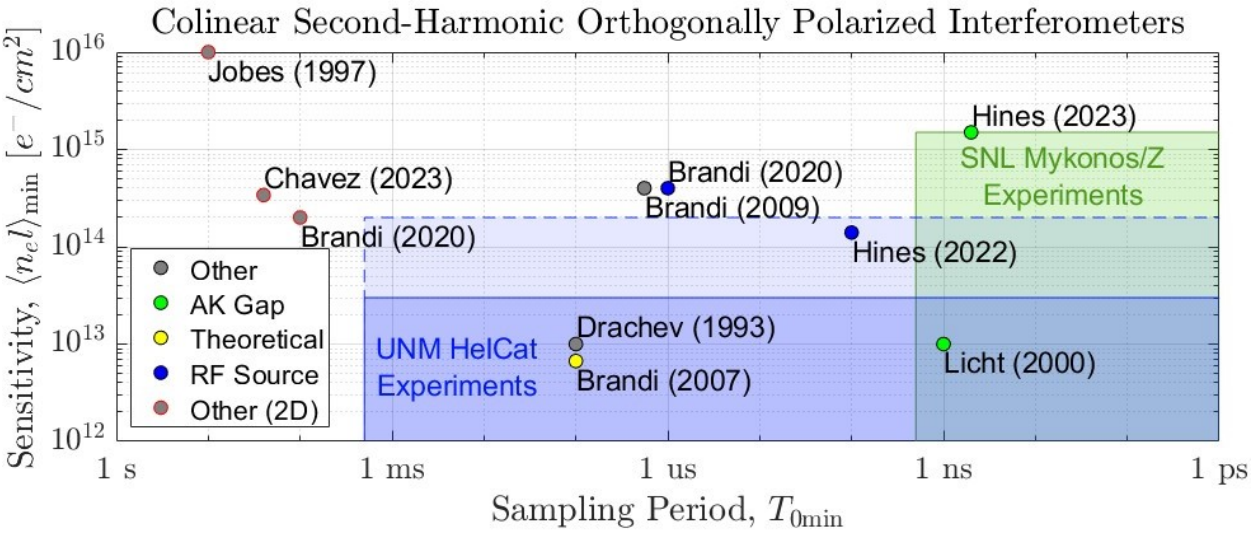

Figure 1.4. All known colinear SHOP interferometers comparison plot. Differences are shown between diagnostic sensitivity (lowest capable areal density measurement), time resolution (maximum sample rate), and plasma source used. Boxed regions highlight the required sensitivity and sample rate to make accurate plasma areal density measurements of (solid blue) UNM HelCat single-shot, (dashed blue) UNM HelCat utilizing multi-shot averaging, and (green) SNL's Mykonos and Z MITLs.

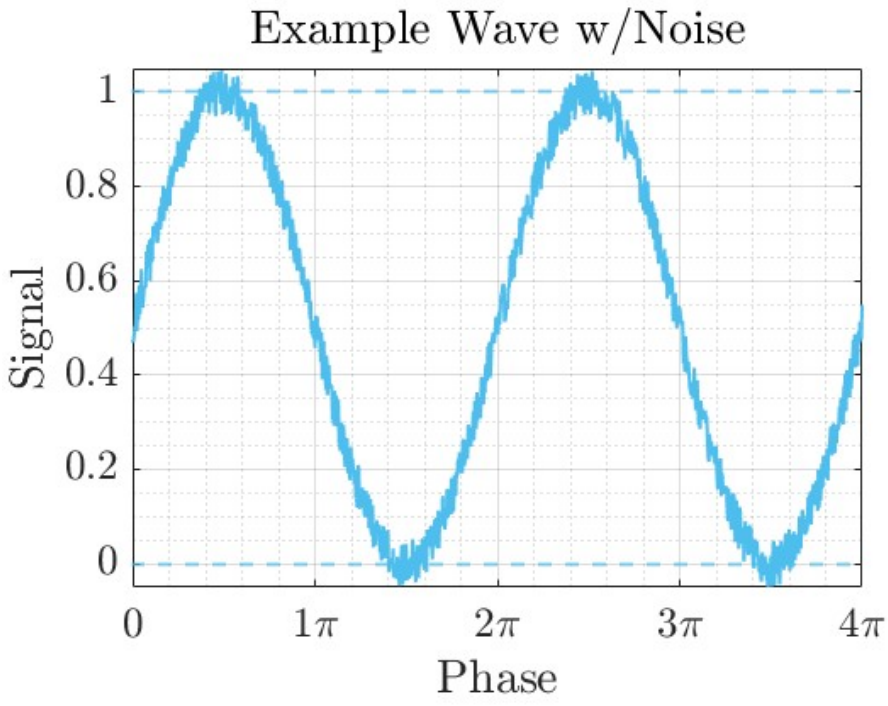

Figure 1.5. Example sin wave plotted with the signal-to-noise ratio obtained by Hines (2022) [20] and Hines (2023).

2. POWER FLOW FUNDAMENTALS

This chapter highlights the fundamental physical principles driving current loss and plasma behavior in high-current-density electrode A-K gaps. It discuss two main topics: (1) particle emission from pulsed transmission lines, and (2) basic plasma parameters. The goal is to provide an outline of why and how charged particles are liberated and behave inside MITLs. This should help to better emphasis the motivation behind certain design choices applied to the colinear SHOP interferometer which are discussed in the remaining chapters.

2.1. Particle Emission in Pulsed Transmission Lines

Particle emission from electrode surfaces occurs in three main stages, represented in Fig. (2.1).

(1) There is a voltage pulse on the transmission line generating a cross gap electric field $\vec{\boldsymbol{E}}$ exceeding the electron emission threshold ($240\,\mathrm{kV/cm}$) and electrons are stripped from the cathode. During this initial period machine current is low, magnetic insulation is weak, and the electrons bombard the anode heating its surface.

(2) The voltage pulse drives the machine current up, leading to Joule heating of both electrode surfaces. The electrode current generates an insulating magnetic field, reducing cross gap flow of charged particles.

(3) The electrode temperature exceeds 400°C, leading to ion and neutral desorption into the gap.

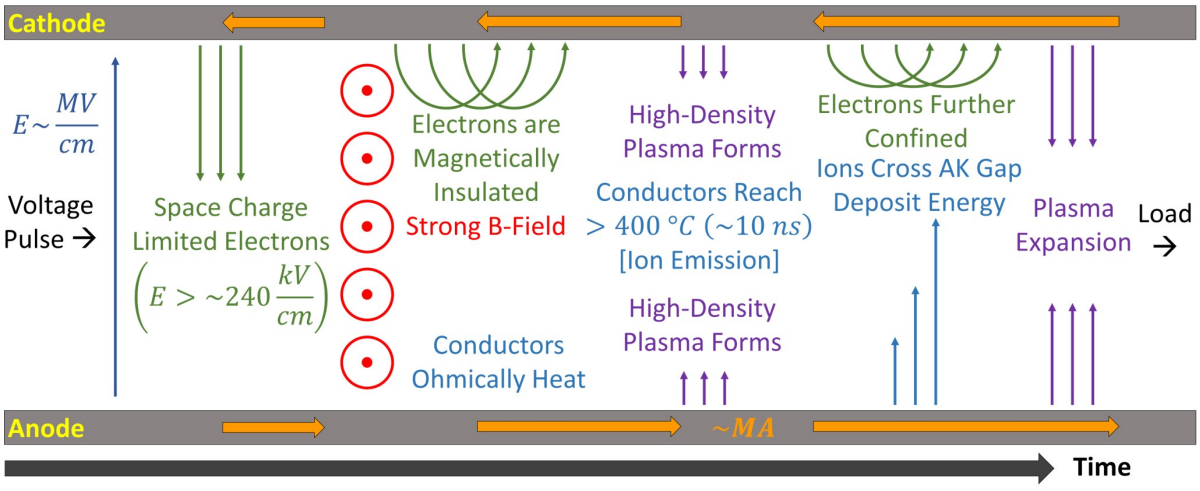

Figure 2.1. Phenomenological diagram of a lossy Magnetically Insulated Transmission Line (MITL). Time moves forward scanning from left to right.

The details of electron, ion, and neutral particle emission are discussed in the following subsections.

2.1.1. Electron Emission

The physics governing electron emission from materials spans many topical research areas and is still an area of active research [24]. The Fowler-Nordheim-type (FN-type) and Murphy-Good (MG) models describe electron emission below the Space-Charge-Limited (SCL) emission. However, the simplification made for MITLs is that there is no significant electron emission until the electric field threshold ($240\,\mathrm{kV/cm}$) is exceeded, after which the electrons are emitted at the SCL emission rate. The SCL emission current density $J_{q,SCL}$ for particles with charge q and mass m, assuming a parallel plate geometry containing a gap spacing distance d in meters and gap voltage V in Volts, is given [25] as

$$\begin{aligned} J_{q,SCL}\left[\mathrm{A\,m^{-2}}\right] &= \frac{4}{9}\varepsilon_0\sqrt{\frac{2q}{m}}\frac{V^{3/2}}{d^2}\,, \\ &= \left(2.33\times10^{-6}\left[\mathrm{F C^{1/2}\,m^{-1}\,kg^{-1/2}}\right]\right)\frac{V^{3/2}}{d^2}\,. \end{aligned} \tag{2.1}$$

The CHICAGO code simulations of inner MITL regions to date use this SCL emission rate from the cathode surface until the local field is canceled out. The SCL emission rate can be exceeded when the electron emission is enhanced by the formation of high density quasi-neutral electrode surface plasmas, which has the effect of closing the gap and increasing the electric field strength.

2.1.2. Particle Energy Deposition & Joule Heating

The *Kinetic Energy KE* of an electron having crossed a parallel plate A-K gap is relativistic and given as

$$KE = \left[\frac{1}{\sqrt{1-\dfrac{v^2}{c^2}}} - 1\right] mc^2 = Ve^-\,, \tag{2.2}$$

where v is the electron's velocity, c is the speed of light, V is the voltage across the A-K gap, and e^- is the charge of an electron.

The anode's surface heating from electron bombardment (assuming the electron current density is J_e), can be calculated if one knows the anode material's specific heat c_v, density ρ, molar mass M, and stopping power $\delta KE/\delta x$. The change in anode surface temperature ΔT is thus

$$\Delta T = \left(\frac{MJ_e}{c_v\rho}\right)\frac{\delta KE}{\delta x}\,. \tag{2.3}$$

Joule's law of heating says that the heating power P generated by a conductor is the product of the square of the current I^2 and the resistance R. Heat Q is just the amount of power deposited over some duration, therefore

$$Q = I^2 R t \,. \tag{2.4}$$

However, pulsed A-K gap electrode's local current flow and material resistance is not entirely understood.

2.1.3. Ion & Neutral Emission

Neutral desorption in A-K gaps with electric field strengths of 240 - 5000 kV/cm occurs once the anode surface reaches temperatures above $400\,^{\circ}C$ [26]–[29], but recent experimental studies (personal correspondence) have shown anode ion stripping occurring at electric field strengths exceeding 10000 kV/cm when the electrode surface is still below temperatures of 400 °C.

Similar to electron emission, there is an SCL ion emission threshold given by Eq. (2.1). However, the emitted ion current density can also be enhanced above the SCL limit by the formation of a high density electron sheath acting as a virtual cathode [30]. In TW-class accelerators, it is thought that this enhancement factor can increase the ion emission current density to several tens of times larger than the SCL emission.

2.1.3.1. Stainless Steel Monolayer

To estimate A-K gap plasma densities, knowledge of the number of allowable particles which can contribute to the plasma from the electrodes is needed. The electrode surface impurities' and contaminates' effect on this number density is still not completely known. Therefore, estimation of the maximum number of desorbable monolayers is accomplished by running multiple PIC simulations, each with varying number of maximum desorbable monolayers defined, and picking the simulation that matches experimentally measured current loss.

As an example of the estimation of a monolayer, the type of A-K electrode material used throughout our experiments was austenitic SAE-304L Stainless Steel (SS), which has an average atomic volume of $V_a = 0.0071\,\mathrm{m}^3/\mathrm{kmol}$. The atomic density ρ is calculated by

$$\rho = \frac{1{,}000 * 6.02 \times 10^{23}}{V_a} \,. \tag{2.5a}$$

Therefore, the atomic density of SAE-304L is

$$\rho = 8.48 \times 10^{28} \left[\mathrm{particles}/\mathrm{m}^3\right] .$$

304L has a Face-Centered Cubic (FCC) crystalline structure, with 14 particles per unit cell, shown in Fig. (2.2a).

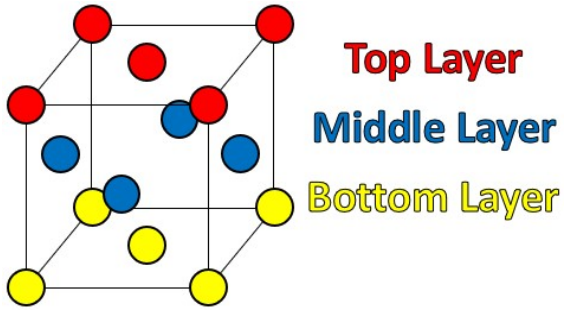

(a)

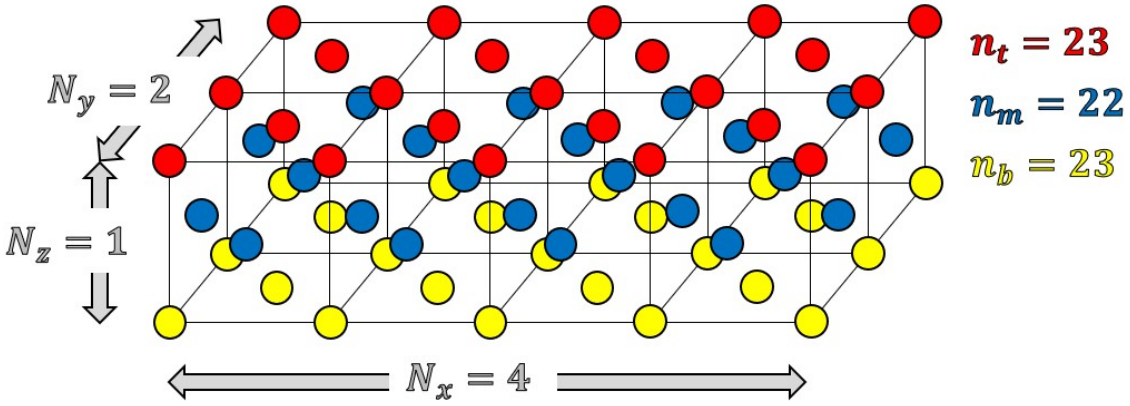

(b)

Figure 2.2. Example images of (a) FCC unit cell structure, and (b) $4 \times 2 \times 1$ **FCC cells structure.**

There are $N \times N \times N$ unit cells in a cubic meter of material, where N is solved (for FCC unit cells) by finding the roots of the following equation

$$\rho = (N+1)\left[(N+1)^2 + N^2\right] + N\left[2N(N+1)\right], \tag{2.6a}$$

or equivalently

$$0 = 4N^3 + 6N^2 + 3N + (1-\rho), \tag{2.6b}$$

the solution of which for 304L is

$$N = 2.79 \times 10^9 \text{ [unit cells]}.$$

In one square centimeter of SAE-304L SS surface, the average number of particles on the crystalline top face atomic layer is

$$\rho_A = \left(\frac{N}{100} + 1\right)^2 + \left(\frac{N}{100}\right)^2, \tag{2.7a}$$

$$\rho_A \approx \frac{N^2}{5,000}, \tag{2.7b}$$

leading to the definition of a monolayer (the same as the estimate of the number of particles in a square centimeter one atom thick), of SAE-304L SS as

$$\rho_A = 1.56 \times 10^{15} \left[\text{particles/cm}^2\right] .$$

When N is significantly large, the number of particles in the top and bottom layer of a single unit cell thick is approximately equal to the number in the middle layer. Therefore, the definition of a monolayer is the same whether referencing the top layer, second layer, third layer, and so on.

To calculate the volumetric density once n number monolayers are desorbed, simply divide the number of monolayers' surface density by the distance of the vacuum volume normal to the surface

$$\rho_V = \frac{n\rho_A}{d_\perp} . \tag{2.8}$$

As an example, if one monolayer of SAE-304L SS was desorbed from an electrode surface into a surrounding 0.2 mm thick volume, there would be a particle density of:

$$\rho_V \left(d_\perp = 0.02 \left[\text{cm}\right]\right) = 7.8 \times 10^{16} \left[\text{particles/cm}^3\right] ,$$

leading to an areal (line-averaged) density measurement made by the colinear SHOP interferometer of $7.8 \times 10^{16}\,\text{cm}^{-2}$. Notably, if double the number of monolayers (two layers) desorbed into a surrounding volume twice as thick (0.4 mm), then there would be no difference in the detected areal density of the interferometer. Therefore, to correlate the interferometer's areal density measurement to some number of desorbed monolayers, an understanding of the density gradient across the A-K gap is needed.

However, the electrode surfaces are typically covered with surface impurities, such as iron oxides and water [28], [31]. These surface impurities have an increased monolayer surface density definition, closer to 3 - $8 \times 10^{15}\,\text{cm}^{-2}$.

2.2. Plasma Parameters

Plasmas have a wide range of particle densities, so they can behave like a high density fluid or a low density collection of individual particles. The A-K gap region contains prescribed $\vec{\boldsymbol{E}}$ and $\vec{\boldsymbol{B}}$ fields not generated by the plasma alone, so we consider some of the plasma parameters that arise as an effect (single-particle motions), as well as internal charge arrangements (plasma as a fluid).

2.2.1. Particle Oscillations

The phenomenon of the circular gyration of a particle having charge q and mass m around a prescribed magnetic field $\vec{\boldsymbol{B}}$ happens at the *cyclotron frequency* ω_c given by

$$\omega_c = \frac{|q|\vec{\boldsymbol{B}}}{m} , \tag{2.9}$$

occurring with a *cyclotron radius* (or *Larmor radius*) of

$$r_L = \frac{mv_\perp}{qB}, \tag{2.10}$$

where the perpendicular linear velocity $v_\perp = r_L\omega_c$. The Larmor gyration is shown in Fig. (2.3b).

The *plasma frequency*, ω_p, is the characteristic frequency of the quasi-neutral plasma's free electron oscillation around their equilibrium position, and is given by

$$\omega_p = \sqrt{\frac{n_e e^2}{\varepsilon_0 m_e}}, \tag{2.11}$$

where n_e is the electron number density, e is the electron charge, ε_0 is the permittivity of free space, and m_e is the mass of an electron. This plasma frequency is so fast that the heavy ions do not have time to respond and are considered fixed. The electron oscillation is shown in Fig. (2.3a). The plasma frequency derivation assumes several things; (1) The background magnetic field is zero, (2) there are no thermal motions $(KT = 0)$, (3) the ions are fixed and uniform, (4) the plasma is infinite in extent, and (5) the electron oscillations occur only in the disturbing electric field direction.

A plasma reaches a *cutoff* condition when its plasma frequency ω_p equals an internal propagating electromagnetic wave's frequency ω, like that of an interferometer's probing laser beam frequency. Any probing beam greater than or equal to the critical plasma density n_c will not transmit through the plasma. The critical plasma density is derived from Eq. (2.11) as

$$n_c = \frac{m_e \varepsilon_0 \omega^2}{e^2}. \tag{2.12}$$

Note:

$$\begin{aligned} n_c\,(\lambda = 1550\,\mathrm{nm}) &= 4.64 \times 10^{20}\,\mathrm{cm}^{-3}, \\ n_c\,(\lambda = 775\,\mathrm{nm}) &= 18.56 \times 10^{20}\,\mathrm{cm}^{-3}. \end{aligned}$$

For electron oscillations propagating at right angles to a nonzero magnetic field, there arises an *upper hybrid frequency* ω_h resulting from both a plasma oscillation ω_p and a Larmor gyration ω_c. This effectively converts the electron motion into ellipses around the magnetic field lines and stretched with it's semi-major axis parallel to the electric field, shown in Fig. (2.3). ω_h is given as

$$\omega_h = \sqrt{\omega_p^2 + \omega_c^2}. \tag{2.13}$$

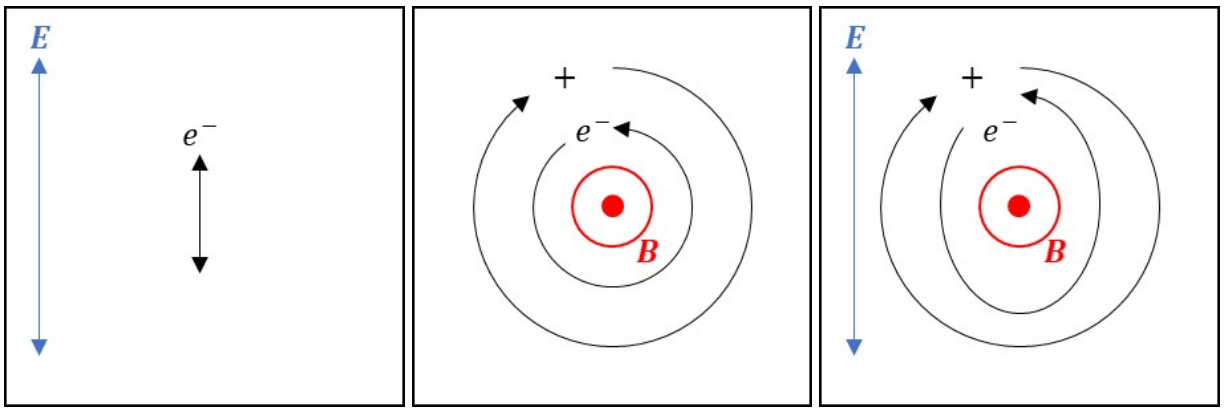

(a) Plasma oscillation (b) Larmor gyration (c) Hybrid

Figure 2.3. Charged particle oscillations due to electric and magnetic fields.

2.2.2. Particle Drifts

In the case where there is a continuous background electric and magnetic field (like the hybrid model described above), there is an additional "drifting" force on both negative and positive charged particles in the $\vec{\boldsymbol{E}} \times \vec{\boldsymbol{B}}$ direction. The associated $\vec{\boldsymbol{E}} \times \vec{\boldsymbol{B}}$ *drift velocity* magnitude is given as

$$|\vec{\boldsymbol{v}}_E| \ (\mathrm{m/s}) = \frac{E \ (\mathrm{V/m})}{B \ (\mathrm{T})} \tag{2.14}$$

The drift velocity is independent of the particles charge or mass. Fig. (2.4) shows example drift velocities for a variety of electric and magnetic fields common to the inner MITLs of *Z*. For MITL geometries, the electric field direction is from the anode (positive charge) to the cathode (negative charge), and the magnetic field direction follows the right-hand-rule from the current flow direction. This leads to an $\vec{\boldsymbol{E}} \times \vec{\boldsymbol{B}}$ drift of all charged particles downstream towards the load, shown in Fig. (2.5).

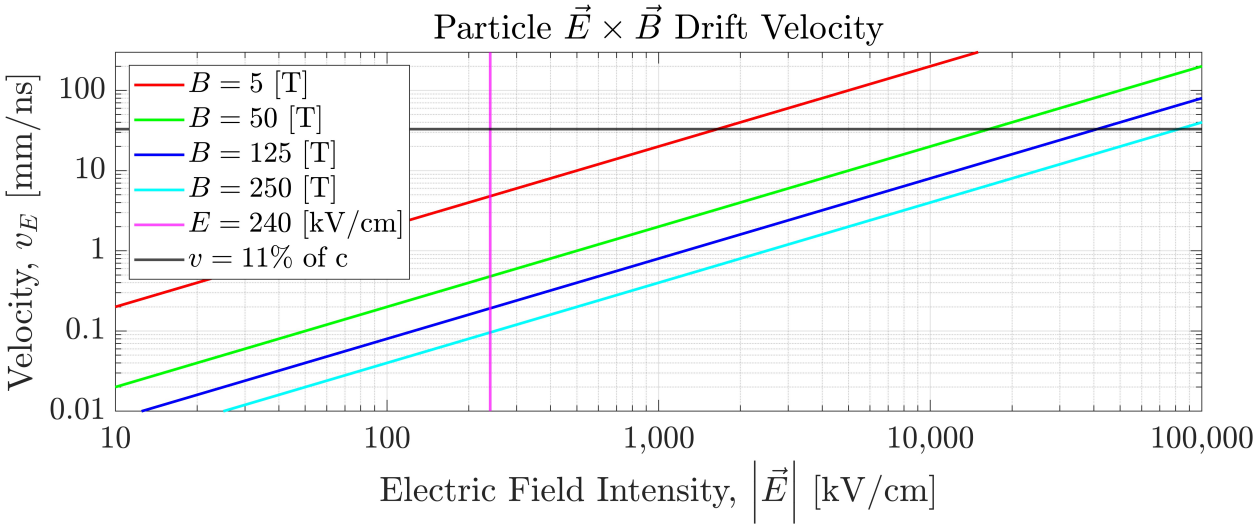

Figure 2.4. Particle drift velocity plot for varying electric and magnetic field intensities that are typical to pulsed MITL regions. A magenta line marks the electron emission threshold field strength, and a black line marks the velocity that is 11% the speed of light and relativistic effects need to be accounted.

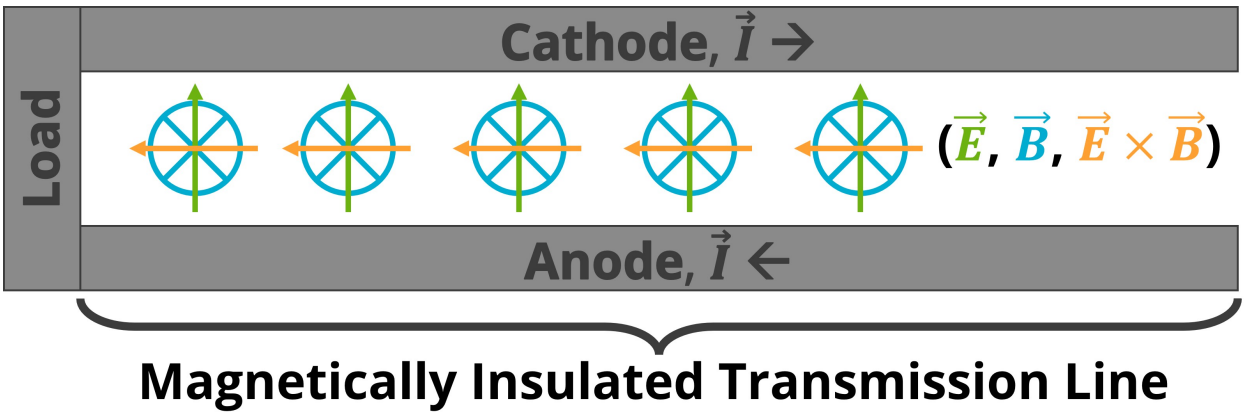

Figure 2.5. Parallel plate A-K gap geometry highlighting the electric field direction from the positively charged anode to the negatively charged cathode, the magnetic field direction following the right-hand-rule from current flow, and the $\vec{E} \times \vec{B}$ direction downstream towards the load region.

2.2.3. Dispersion Relations

The dispersion relations correlate the plasma's measured refractive index $\widetilde{n}$ to physical properties like its particle density and the probing beam's wavelength. There are three dispersion relations, shown in Table (2.1), categorized by how a linearly polarized probing beam's propagation ($\vec{k}$ and $\vec{E}$) relates to a background magnetic field ($\vec{B}$).

Dispersion Relations		
O Wave:	$\vec{k} \perp \vec{B}$, $\vec{E} \parallel \vec{B}$ or $B = 0$	$\widetilde{n}^2 = 1 - \dfrac{\omega_p^2}{\omega^2}$
X Wave:	$\vec{k} \perp \vec{B}$, $\vec{E} \perp \vec{B}$	$\widetilde{n}^2 = 1 - \dfrac{\omega_p^2}{\omega^2}\left(\dfrac{\omega^2 - \omega_p^2}{\omega^2 - \omega_h^2}\right)$
R-L Wave:	$\vec{k} \parallel \vec{B}$	$\widetilde{n}^2 = 1 - \dfrac{\omega_p^2/\omega^2}{1 - (\omega_c/\omega)}$ (R Wave) $\widetilde{n}^2 = 1 - \dfrac{\omega_p^2/\omega^2}{1 + (\omega_c/\omega)}$ (L Wave)

Table 2.1. The three (O, X, and R-L) waves dispersion relations relating refractive index to plasma and beam parameters.

The simplest geometry (called *O Wave* or *O mode* propagation) is when either there is no background magnetic field or the probing beam propagates perpendicular to the background magnetic field and the beam's electric field is parallel to the background magnetic field. The magnetic field has no effect on the dispersion relation for O mode propagation. If the probing beam's electric field were also perpendicular to the background magnetic field, then we consider the propagating geometry to be *X mode* and the dispersion relation is modified. In the case where the probing electromagnetic beam is propagating parallel to the magnetic field $\vec{k} \parallel \vec{B}$ (called *R-L Wave* propagation), there are two dispersion relations effecting a right and left hand circular polarization. The superposition of the R-L waves leads to a Faraday effect where the polarization angle of linearly polarized light rotates as it passes through the plasma.

The rotation angles of a 1550 nm wave traveling through 2 mm of plasma with varying background magnetic fields is shown as a function of the uniform plasma density in Fig. (2.6). We prefer minimal Faraday rotation of the colinear SHOP interferometer's beams, since their polarization angle dictates SH generation (discussed further in Sec. (3.2)), as well as the splitting for detection and analysis (discussed further in Sec. (3.3)).

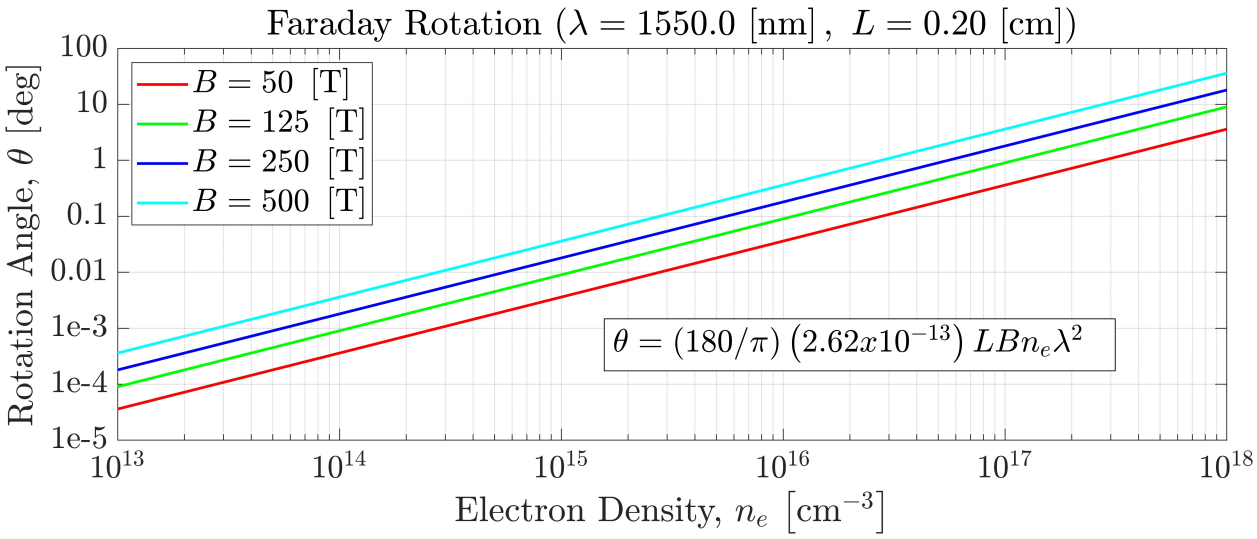

Figure 2.6. Plot of the Faraday polarization rotation angle of a $1550\,\mathrm{nm}$ wave traveling along a $2\,\mathrm{mm}$ path length of a plasma with some constant electron density. Several line are shown with respective magnetic flux densities.

3. COLINEAR SHOP INTERFEROMETER DIAGNOSTIC

This chapter will discuss the SHOP interferometer diagnostic generally and highlight its necessary components; including the laser source, Second-Harmonic (SH) crystals, and detectors. The general design layout of the system used throughout this project is shown in Fig. (3.1).

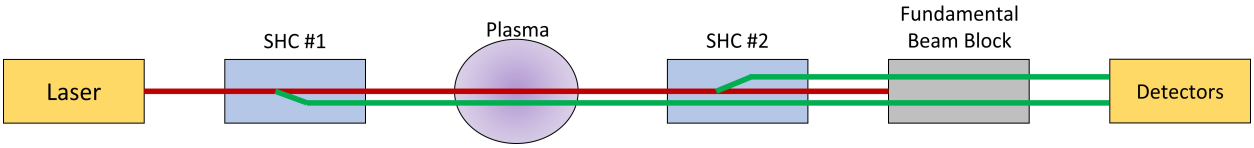

Figure 3.1. Colinear SHOP interferometer general design. Shown are all necessary components including the laser source, SH Crystals (SHC), and detector(s).

A laser source's First-Harmonic (or "Fundamental-Harmonic") (FH) wave is passed through a SH crystal which converts a portion of the FH wave into a frequency doubled SH wave. Efficient conversion of the FH into the SH is discussed further in Sec. (3.2). The two FH and SH waves have constant relative phase and propagate along identical optical paths, therefore they are *colinear*.

Both the FH and SH waves pass through the plasma, however they experience different phase delays due to the wavelength dependent refractive index. The wavelength dependence on index of refraction was shown in Table (2.1), and it's effect on phase change is shown later in Eq. (3.6). The relative phase change, via *dispersion*, is why this is often referred to as a "*dispersion* interferometer" and is the physical principle that enables measurement of the plasma's free-electron density. However, every interferometer takes advantage of dispersion physics, hence the "Second-Harmonic Orthogonal Polarized (SHOP)" specifying distinction made here.

For convenience of detecting a single wavelength and to increase the signal-to-noise ratio, after passing through the plasma a portion of the FH wave is then again frequency doubled to a second SH wave. The FH is no longer needed and is therefore filtered out. The relative phase of the two SH waves is then detected. Detection scheme details are provided in Sec. (3.3).

3.1. Laser Source

The FH wave laser source utilized for this system was the Keopsys CEFL-KILO continuous wave erbium fiber laser. The laser specifications are included in Table (3.1).

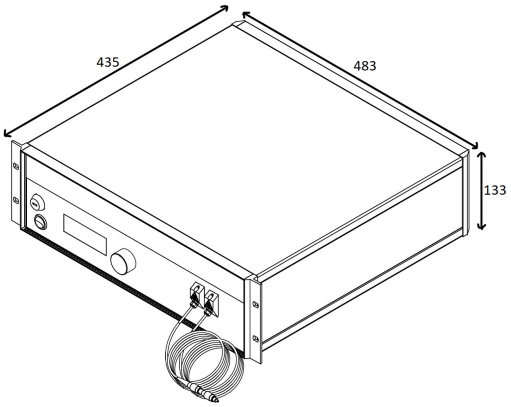

Figure 3.2. CEFL-KILO fiber laser [32].

CEFL-KILO Optical Specifications @ 25 °C	
Mode of Operation	CW
Output Power	From 0.5 to 7 W
Operating Wavelength	1550 ± 2 nm
Spectral Linewidth	5 kHz
Polarization	Linear (17 dB PER)

Table 3.1. CEFL-KILO optical specs @ 25 $^{\circ}C$.

To pass the FH wave through the SH crystals and plasma it must be open beam rather than fiber coupled, so the laser fiber output was terminated with a fiber collimator to propagate a 2 mm open beam. Though this specific fiber laser has a linearly polarized output, we do not inherently know the polarization angle. Therefore, we passed the FH open beam through a half-wave plate to rotate its polarization. Then, the FH beam was filtered via a polarizing beam splitter to measure and guarantee its polarization angle state.

3.2. Second-Harmonic Generation

To generate the SH 775 nm beam from the FH 1550 nm beam, the FH beam was passed through a 25 mm long Periodically Poled Lithium Niobate (PPLN) chip purchased from HC Photonics Corp. A graphic showing the crystal's periodicity is shown in Fig. (3.3) and details of the chip are given in Table (3.2). The magnitude of SH generated is proportional to the square of the FH's electric field.

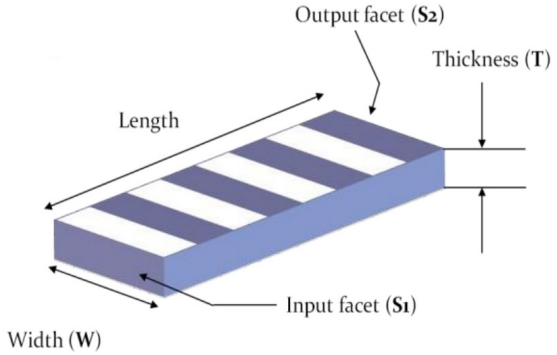

Figure 3.3. SHNIR-SA PPLN chip [33].

SHNIR-SA PPLN chip properties	
Material	5 mol.% MgO:LN
Optical Coating	$R < 0.5\%$ @775 nm $R < 0.3\%$ @1550 nm
Thickness	1 ± 0.05 mm (T)
Width	2 ± 0.1 mm (W)
Length	25 ± 0.2 mm
Clear Aperture	$\geq 80\%$ (T), $\geq 90\%$ (W)

Table 3.2. SHNIR-SA PPLN chip properties.

For higher SH conversion efficiency, the FH was focused through the crystals such that the beam's Rayleigh length was approximately half the crystal length, shown in Fig. (3.4).

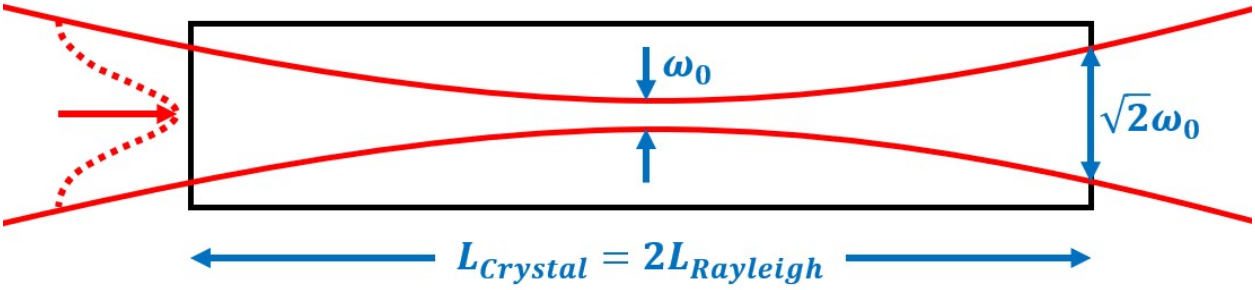

Figure 3.4. Example Rayleigh length focused beam propagation through SH crystal.

SNLO software was utilized to calculate SH conversion and beam propagation parameters assuming the use of 25 mm and 50 mm PPLN crystal lengths. The simulations showed little advantage to using the longer 50 mm long crystal instead of the 25 mm long crystal when using 0.5-5 Watts of FH power. It also proved that the crystals could generate enough SH power for the interferometer's detectors to pick up substantial signal.

3.2.1. Phase Matching

Phase Matching (PM) periodically poled crystals requires adjusting the relative phase between the two wavelengths as they propagate through the crystal. These crystals are PM tuned by varying their operational temperature, which has the effect of varying the crystal's periodic poling length. From the temperature phase matching data, shown in Fig. (3.5), the crystals require $\sim 32\,^{\circ}$C to correctly phase match with the 1550 nm FH and most efficiently convert.

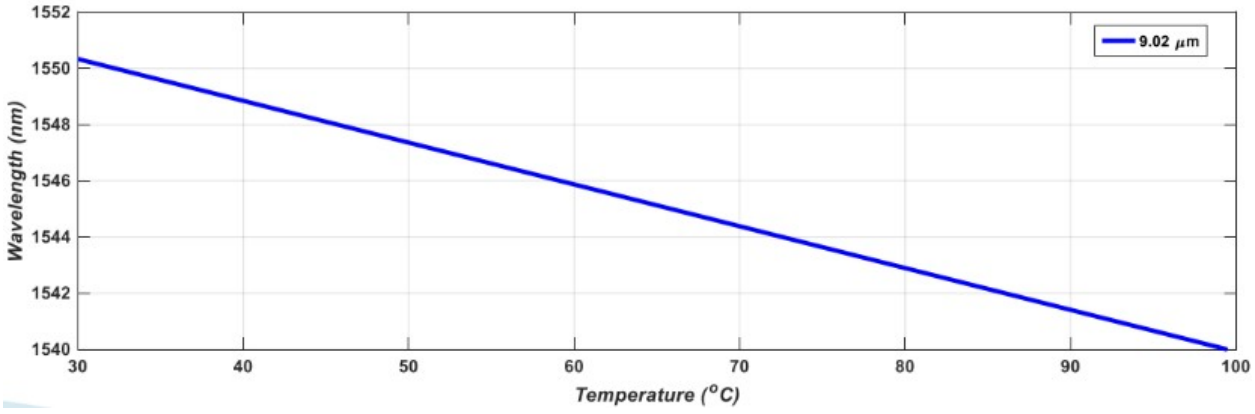

Figure 3.5. SHNIR-SA PPLN chip phase matching tuning curve provided by the manufacturer [33].

The SNLO calculations, shown in Fig. (3.6), output a room temperature crystal poling period of 19.56 μm. Further SNLO inquiry suggests an oven temperature of 61.9 °C is required to bring the poling period back to the manufacture suggested 19.36 μm.

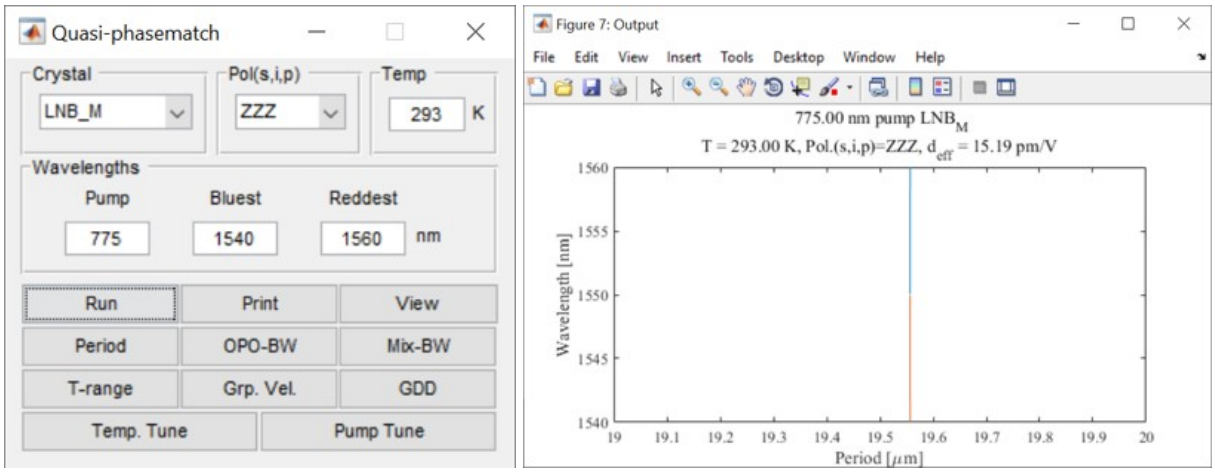

(a) (b)

Figure 3.6. SNLO (a) input and (b) output calculations to phase match .

The PPLN chip crystals were mounted inside of the Heatpoint HP30-3×3 oven manufactured by Eksma Optics, which is specifically designed to heat nonlinear crystals. A graphic showing the oven's dimensions is shown in Fig. (3.7) and the oven specifications are listed in Table (3.3).

Contrary to the SNLO calculations, bench top experiments suggested temperatures between 32 - 42 °C were optimal for SH conversion. However, this could have been caused by the oven's measured/displayed temperature having errors greater than its listed stability. Though there is not experimental data to support this claim, there was a noticeable drift of the oven's measured/displayed optimum conversion temperature over time scales of weeks/months. Over such long periods, the optimum oven temperature continuously drifted upwards, leading to the large 10 °C range listed above.

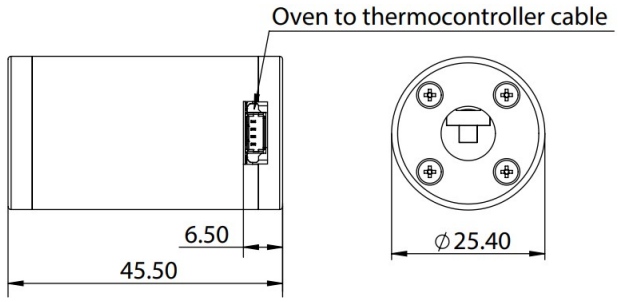

Figure 3.7. Heatpoint oven [34].

HP30-3×3 oven properties	
Crystal Housing	$3 \times 3 \times 30$ mm
Temperature Range	$25 - 70$ °C
Temperature Step	0.1 °C
Stability	± 0.1 °C
Ramp Rate	3 °C/min
Outer Dimensions	$\varnothing 25.4 \times 45.5$ mm
Power Requirements	12 V DC

Table 3.3. Heatpoint oven properties.

The ovens have a $3 \times 3 \times 30$ mm crystal housing, while the crystals measured only $2 \times 1 \times 25$ mm. To improve thermal contact between the larger housing and smaller crystal, we designed a secondary crystal oven housing comprised of a bottom U-shaped holder and top rectangular lid, both made from aluminum for its strength and thermal conductivity, shown in Fig. (3.8). This additional housing mounts the crystal in place at the center of the oven's original housing, helping to preserve optical alignment after crystal rotation around the optical axis.

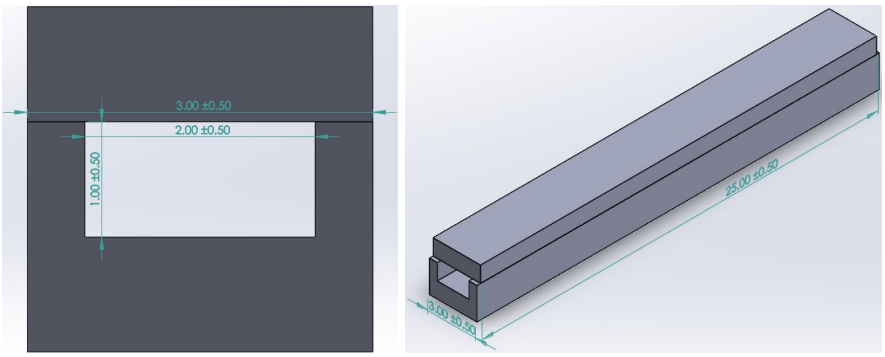

(a) Face View **(b) Isometric View**

Figure 3.8. Second-harmonic crystal oven housing hardware.

3.2.2. Polarization Angle Matching

Bench top experiments showed that the rotation angle of the crystal around the optical axis vs the polarization angle of the FH wave had an effect on the polarization state of the generated SH wave. The strong polarization ("strong" = the polarization angle that is desired) generation function of crystal rotation angle is derived from the following intuitive steps: only the parallel component of the crystal reacts to the input strong polarization wave, leading to a reduction of effective input FH electric field by a factor of $\cos(\theta)$ or an intensity factor of $\cos^2(\theta)$; the SH intensity drops as a function of the input intensity squared due to the *nonlinear* crystal, leading to an output SH intensity factor of $\cos^4(\theta)$. The generated SH polarization is inline with the crystal rotation angle but the strong detector is inline with $\theta = 0\,^\circ$, leading to a further intensity reduction factor of $\cos^2(\theta)$ and a total strong intensity factor of $\cos^6(\theta)$.

The weak ("weak" = the polarization angle not desired) generation function is derived the same way, except that the weak detector is inline with $\theta = 90\,^\circ$, leading to a further intensity reduction factor of $\sin^2(\theta)$ and a total weak intensity factor of $\cos^4(\theta)\sin^2(\theta)$. The experimental data from the first crystal's output, which was meant to produce $\vec{S}$ polarized SH from an $\vec{S}$ polarized FH, matched these expected curves. Our experimental data is plotted overlapped on the expected curves shown in Fig. (3.9).

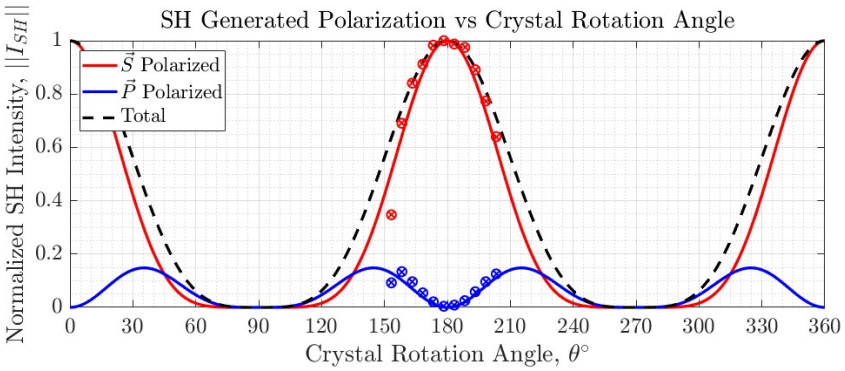

Figure 3.9. Second-harmonic expected output polarization vs crystal axial rotation angle. Overlapped on the plotted curves are markers denoting the experimentally collected data.

Therefore, if the crystal's rotation angle is misaligned off of the FH's polarization axis by $\pm 9.2^{\circ}$, then the total generated SH will be only 95% of the optimal intensity; of that 97.4% will be along the strong axis and 2.6% along the weak axis. For an exaggerated misalignment of 45°, there is only 25% total conversion vs optimal and equal parts of the SH intensity will be polarized along the strong and weak axes. For misalignments $> 45^{\circ}$, there is more SH generation in the weak than in the strong axis.

3.3. Detection Scheme

After the fundamental beam block there are two colinear SH beams (SH_1 & SH_2), which are mutually orthogonal. Their mutual orthogonality is generated with a zero-order $\lambda_{FH}/2 = \lambda_{SH}$ waveplate, shown in Fig. (3.10).

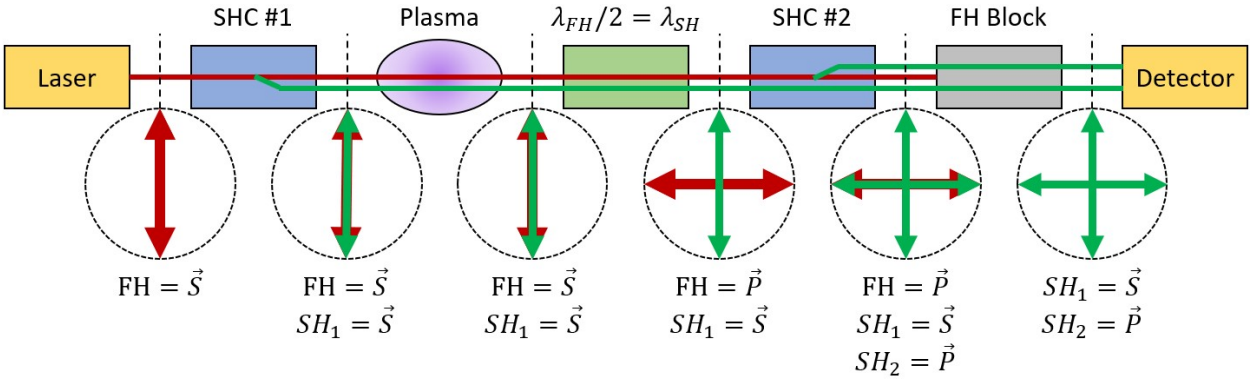

Figure 3.10. SHOP interferometer general design showing the red FH and green SH relative polarization states throughout the optical component layout.

The two orthogonal polarized SH waves are then passed through a polarizing beamsplitter rotated by 45° to split equal components of the SH waves. This splitting generates two waves with respective intensities I_{+45} & I_{-45}. This process is shown in Fig. (3.11).

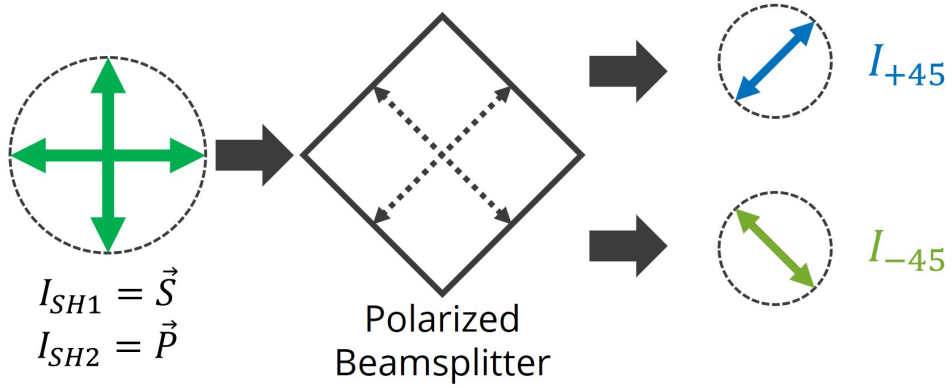

Figure 3.11. Diagram of the colinear SHOP interferometer's SH wave polarization splitting into the two output waves with intensities I_{+45} & I_{-45}.

The two output waves' intensities are a function of the two SH intensities (I_{SH1} and I_{SH2}) as well as the relative phase of the two SH waves ($\Delta\Phi - \phi_0$) via the following equations

$$I_{+45} = \frac{I_{SH1}}{2} + \frac{I_{SH2}}{2} + \sqrt{I_{SH1} I_{SH2}} \cos\left(\Delta\Phi - \phi_0\right), \tag{3.1}$$

$$I_{-45} = \frac{I_{SH1}}{2} + \frac{I_{SH2}}{2} - \sqrt{I_{SH1} I_{SH2}} \cos\left(\Delta\Phi - \phi_0\right). \tag{3.2}$$

The DC offset value ($I_{SH1}/2 + I_{SH2}/2$) can be removed by subtracting the two signals from each other, creating an intensity I_{Diff} which can then have gain applied to only an amplitude component.

$$\begin{aligned} I_{Diff} &= I_{+45} - I_{-45}, \\ &= 2\sqrt{I_{SH1} I_{SH2}} \cos\left(\Delta\Phi - \phi_0\right) \\ &. \end{aligned} \tag{3.3}$$

The change in phase $\Delta\Phi$ of the detected output signals (I_{+45} & I_{-45}) from the DI is a function of the difference in the change of phases of the two SH waves ($\Delta\varphi_{SH,2}$ & $\Delta\varphi_{SH,1}$), given as

$$\Delta\Phi = \Delta\varphi_{SH,2} - \Delta\varphi_{SH,1}. \tag{3.4}$$

The change in phase of the second second-harmonic wave $\Delta\varphi_{SH,2}$ is twice the change in phase of the generating fundamental wave $\Delta\varphi_F$, due to the second-harmonic generation process. Therefore, the change in phase is simply

$$\Delta\Phi = 2\Delta\varphi_F - \Delta\varphi_{SH,1}, \tag{3.5}$$

which can be rewritten as a function of the probing path length L and FH's wave number $k_{0,F}$ via

$$\Delta\Phi = 2Lk_{0,F}\left[\widetilde{n}_{SH} - \widetilde{n}_F\right]. \tag{3.6}$$

For ordinary wave (O wave) propagation, from Table (2.1), the dispersion relation can be input into Eq. (3.6) to get

$$\Delta\Phi = 2Lk_{0,F}\left[\sqrt{1 - \left(\frac{\omega_p^2}{4\omega_F^2}\right)} - \sqrt{1 - \left(\frac{\omega_p^2}{\omega_F^2}\right)}\right], \tag{3.7}$$

which can be rewritten into a similar format from Eqs. (2.11 & 2.12) as a function of densities instead of angular frequencies

$$\Delta\Phi = 2Lk_{0,F}\left[\sqrt{1 - \left(\frac{n_e}{4n_{c,F}}\right)} - \sqrt{1 - \left(\frac{n_e}{n_{c,F}}\right)}\right]. \tag{3.8}$$

We can then apply the following Taylor series for x around the point $x \approx 0$, or equivalently for regions when $\omega_p << \omega$, or equivalently when $n_e << n_c$ (for $\lambda_F = 1550\,\text{nm}$, this linearity assumption holds true at electron densities $n_e \leq 1 \times 10^{19}$ cm^3.)

$$\sqrt{1-x} \approx 1 - \frac{x}{2} - \frac{x^2}{8} - \frac{x^3}{16} - \ldots . \tag{3.9}$$

Using the Taylor series given by Eq. (3.9) to second order, the detected change in phase can be approximated as

$$\Delta\Phi \approx 2Lk_{0,F}\left[\left(1 - \frac{n_e}{8n_{c,F}}\right) - \left(1 - \frac{n_e}{2n_{c,F}}\right)\right], \tag{3.10}$$

which can then be simplified and put into base SI units as

$$\begin{aligned}
\Delta\Phi\ [\text{rad}] &\approx \frac{3e^2}{8m_e\varepsilon_0\pi c^2}\lambda_{0,F}Ln_e\,, \\
&\approx \left(4.227\times10^{-15}\ [\text{m}]\right)(\lambda_{0,F}\ [\text{m}])\,(L\ [\text{m}])\left(n_e\ \left[\text{m}^{-3}\right]\right), \\
&\approx \left(4.227\times10^{-20}\right)(\lambda_{0,F}\ [\text{nm}])\,(L\ [\text{cm}])\left(n_e\ \left[\text{cm}^{-3}\right]\right).
\end{aligned} \tag{3.11}$$

The phase change $\Delta\Phi$ from Eq. (3.11) as a function of electron density n_e is plotted in Fig. (3.12) for a variety of probing path lengths typical available in pulsed MITL geometries. Plotted is a sensitivity limit of 1/10 rad (the certainty in our phase measurement around cos(90°)), due to the diagnostic's achieved signal-to-noise ratio. Phase changes occurring below this limit would not exceed the noise level. Additionally plotted is a sensitivity limit of 1/250 rad, which is the best phase detection accuracy of another colinear SHOP interferometer with similar bandwidth.

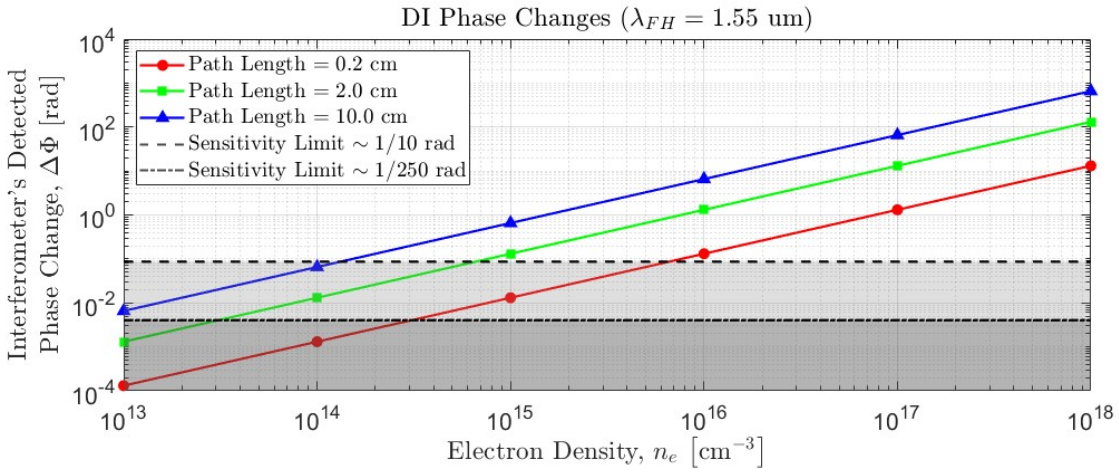

Figure 3.12. Dispersion Interferometer phase change vs electron density.

If lower electron areal density detection sensitivity is desired, there are three variables to adjust: (1) sample more plasma via an increased probing path length; (2) increase the FH wavelength and by consequence the wavelength separation between the FH and SH waves; and/or (3) increase the

signal-to-noise ratio with increased SH intensity or reduced detector noise, thereby increasing the phase detection accuracy.

Since this is a line-averaged measurement, it's simpler to represent the density measurement as an areal density $\langle n_e L \rangle$ which is a linear function of the colinear SHOP interferometer's detected phase change $\Delta\Phi$ as

$$\begin{aligned}\left(\langle n_e L\rangle \ \left[\mathrm{cm}^{-2}\right]\right) &\approx \frac{1}{\left(4.227\times 10^{-20}\right)\left(\lambda_{0,F}\ [\mathrm{nm}]\right)}\left(\Delta\Phi\ [\mathrm{rad}]\right), \\ &\approx \frac{\left(2.366\times 10^{19}\right)}{\left(\lambda_{0,F}\ [\mathrm{nm}]\right)}\left(\Delta\Phi\ [\mathrm{rad}]\right).\end{aligned} \tag{3.12}$$

Note:

$$\begin{aligned}&\langle n_e L\rangle\left(\lambda_{0,F}=1550\ [\mathrm{nm}],\ \Delta\Phi=2\pi\ [\mathrm{rad}]\right)=9.56\times 10^{16}\ \mathrm{cm}^{-2}\\ &\langle n_e L\rangle\left(\lambda_{0,F}=1550\ [\mathrm{nm}],\ \Delta\Phi=0.1\ [\mathrm{rad}]\right)=1.53\times 10^{15}\ \mathrm{cm}^{-2}\end{aligned}$$

It's shown in Fig. (3.13) that this has the effect of shifting all three response curves varying as a function of plasma path length from Fig. (3.12) into one single response curve.

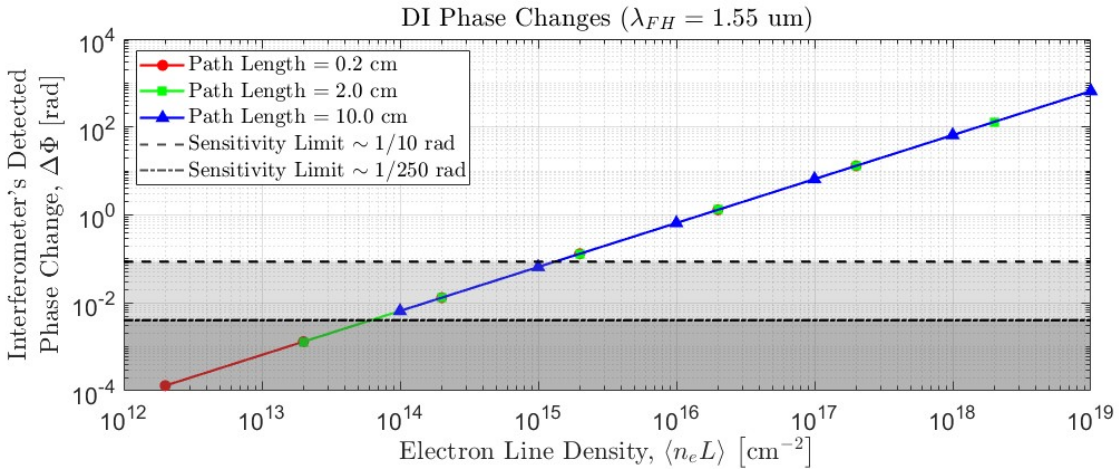

Figure 3.13. Dispersion Interferometer phase change vs electron areal (line-averaged) density.

4. HELCAT EXPERIMENTS

Before taking the newly developed and untested colinear SHOP interferometer to measure the uncertain range and potentially variable (shot-by-shot) electron densities in pulsed MITLs, the diagnostic was instead initially fielded on the well characterized and highly repeatable (shot-by-shot) Radio Frequency (RF) plasma generated by the University of New Mexico (UNM) Helicon-Cathode (HelCat) device, shown in Fig. (4.1). Here, the colinear SHOP interferometer's functionality was verified against a 94 GHz mm-wave interferometer and historic HelCat data from Ref. [35]. The colinear SHOP interferometer's work on the UNM HelCat device lead to a Review of Scientific Instruments (RSI) publication [20], DOI:10.1063/5.0101687.

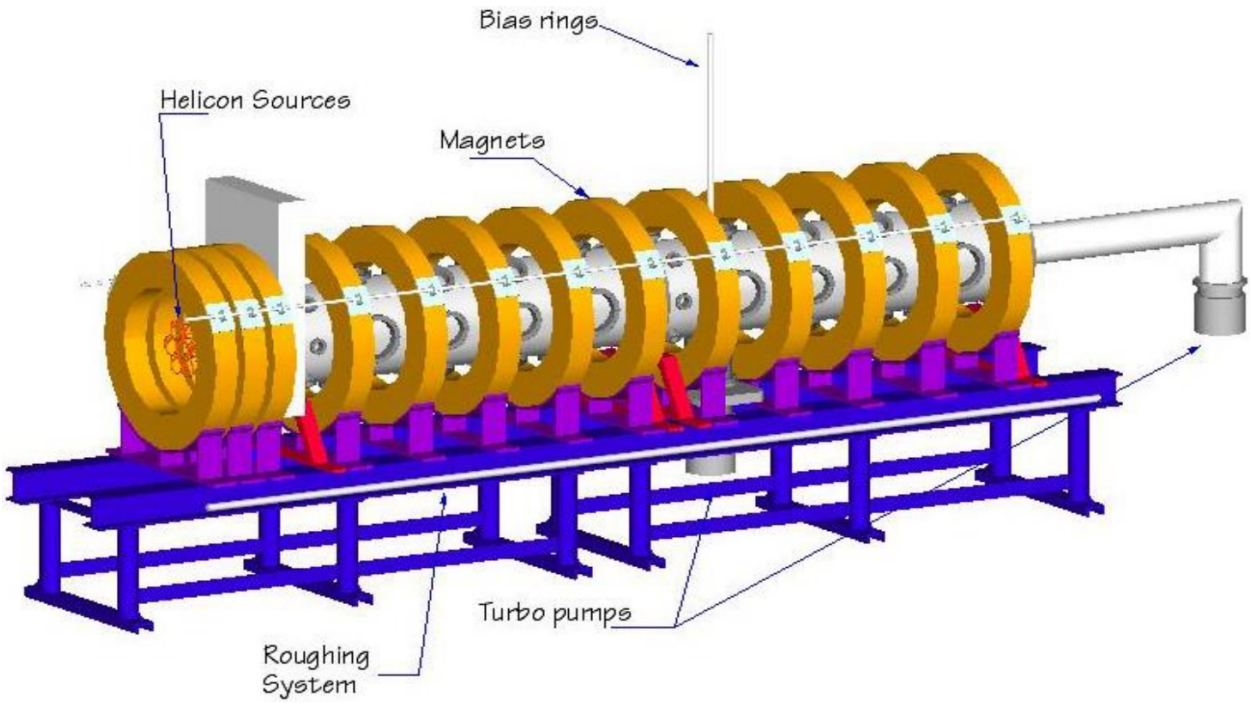

Figure 4.1. Schematic of the University of New Mexico Helicon-Cathode (HelCat) plasma device [35].

The 94 GHz (mm wavelength) interferometer has a longer probing beam wavelength than the SHOP interferometer (VIS/NIR wavelengths), and thus experienced a larger signal phase change when subjected to the same plasma electron line-density, hence the 94 GHz interferometer is more sensitive to lower electron line-densities than the SHOP interferometer. The main downside of the 94 GHz interferometer is due to its longer wavelength, leading to its minimum focused spot size to be significantly larger than the colinear SHOP interferometer's collimated optical beam and exceeding the A-K gap spacing typical of inner MITL regions.

The commissioning of the colinear SHOP interferometer on the HelCat plasma source established confidence that the diagnostic functioned correctly and that it accurately measured the electron line-density of the RF plasma for several reasons:

(1) The SHOP interferometer's areal density measurement matched the 94 GHz interferometer's within 9%, despite there difference in probing beam widths.

(2) The data shown from both interferometers in Fig. (6) of Ref. [20] matches the helicon ion saturation current time resolution curve from Fig. (4) of Ref. [35].

(3) The calculated absolute density SHOP interferometer data also matches the cited peak profile electron densities of $\sim 5 \times 10^{13}\,\mathrm{cm}^{-3}$ given in Ref. [35]. The transition from the SHOP interferometer's line-density [cm^{-2}] data to the absolute spatially resolved density [cm^{-3}] was possible by taking density distribution measurements via a position sweeping double Langmuir probe.

5. INTERFEROMETER'S MITL PLASMA MEASUREMENTS AT MYKONOS

After verification of the colinear SHOP interferometer's functionality on HelCat and gaining confidence in its capability for areal density measurements of MITL plasmas, the diagnostic was brought to the Sandia National Laboratories (SNL) Mykonos facility [36], shown in Fig. (5.1). Here, the diagnostic was fielded on an existing parallel plate A-K gap hardware geometry which added challenges for the diagnostic to measure a plasma density that, compared to the HelCat plasma, was developing in significantly shorter time periods and had a lack of reproducibility. However, with various system improvements, the colinear SHOP interferometer was successfully able to make the first temporal areal density measurement of the generated parallel plate A-K gap plasmas.

Figure 5.1. The SNL Mykonos facility [36]. On the left of the image is the machines charging power supplies, located in white electronic racks. The five vertically orientated disks are the machine's cavities, rendered for a better view in Fig. (5.2). The white room located in front of the five cavities is the Laser Controlled Area (LCA) and is where the vacuum chamber is located.

5.1. Mykonos Pulsed Power Accelerator

The Mykonos Linear Transformer Driver (LTD) is comprised of five cavities, rendered in Fig. (5.2), and is nominally a 500 GW (1 MA, 500 kV) accelerator when charged to 100 kV. The rise times and peak current vary depending on the load impedance and charge voltage. Experiments discussed in this LDRD used a 70 kV charge voltage, resulting in a peak current near 800 kA with an 85 ns rise time. A representative current pulse is shown in Fig. (5.3).

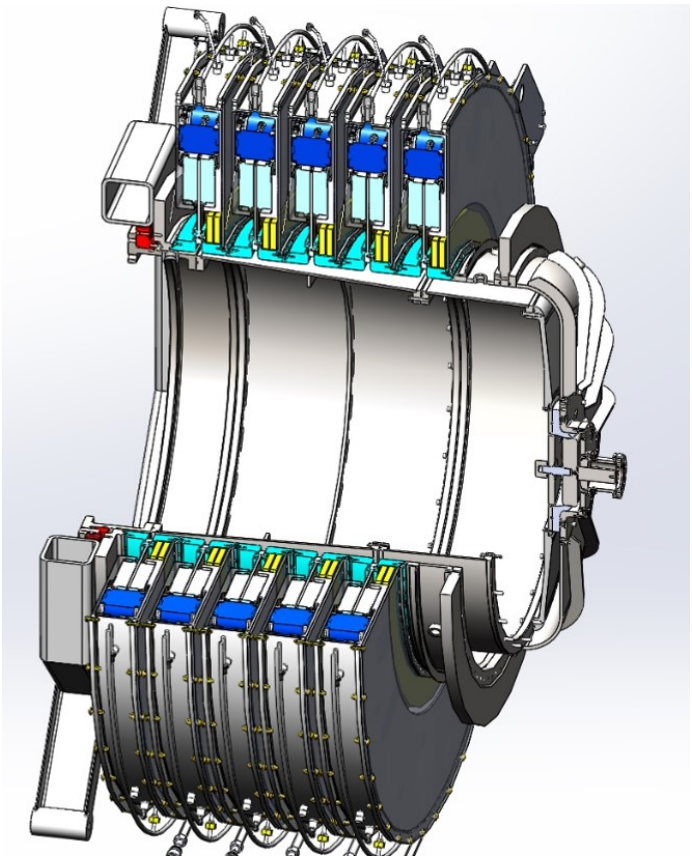

Figure 5.2. Rendering of Mykonos' five LTD cavities (the five rings) driving a water filled coaxial transmission line along its center.

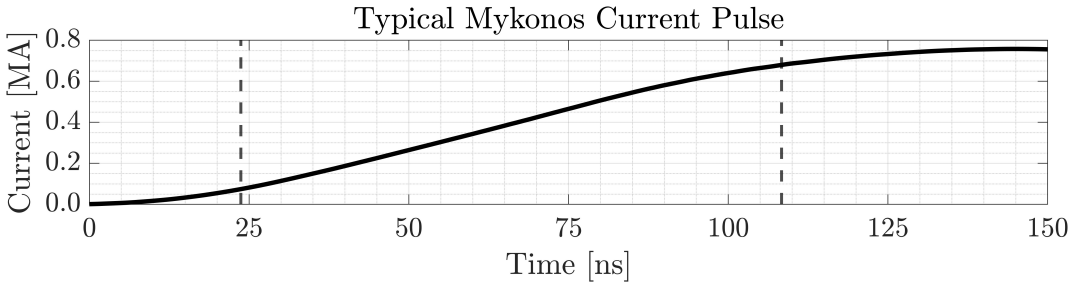

Figure 5.3. Plot of a typical Mykonos LTD current pulse when charged to 70 kV and used for the parallel plate hardware described below.

5.2. AK Gap Hardware Design

The plasma formation experimental mounting hardware used for the colinear SHOP interferometer's Mykonos campaigns are shown in Fig. (5.5) on page (41). The hardware is installed onto the machine's anode and cathode plates via spacer columns, allowing the parallel plate region to be viewed through the vacuum chamber view-ports.

The hardware design allows easy transition between various anode and cathode rods, allowing for variation in parallel plate A-K gap geometry. Both of the parallel plate A-K rod geometries that were implemented with the colinear SHOP interferometer are shown in Fig. (5.4).

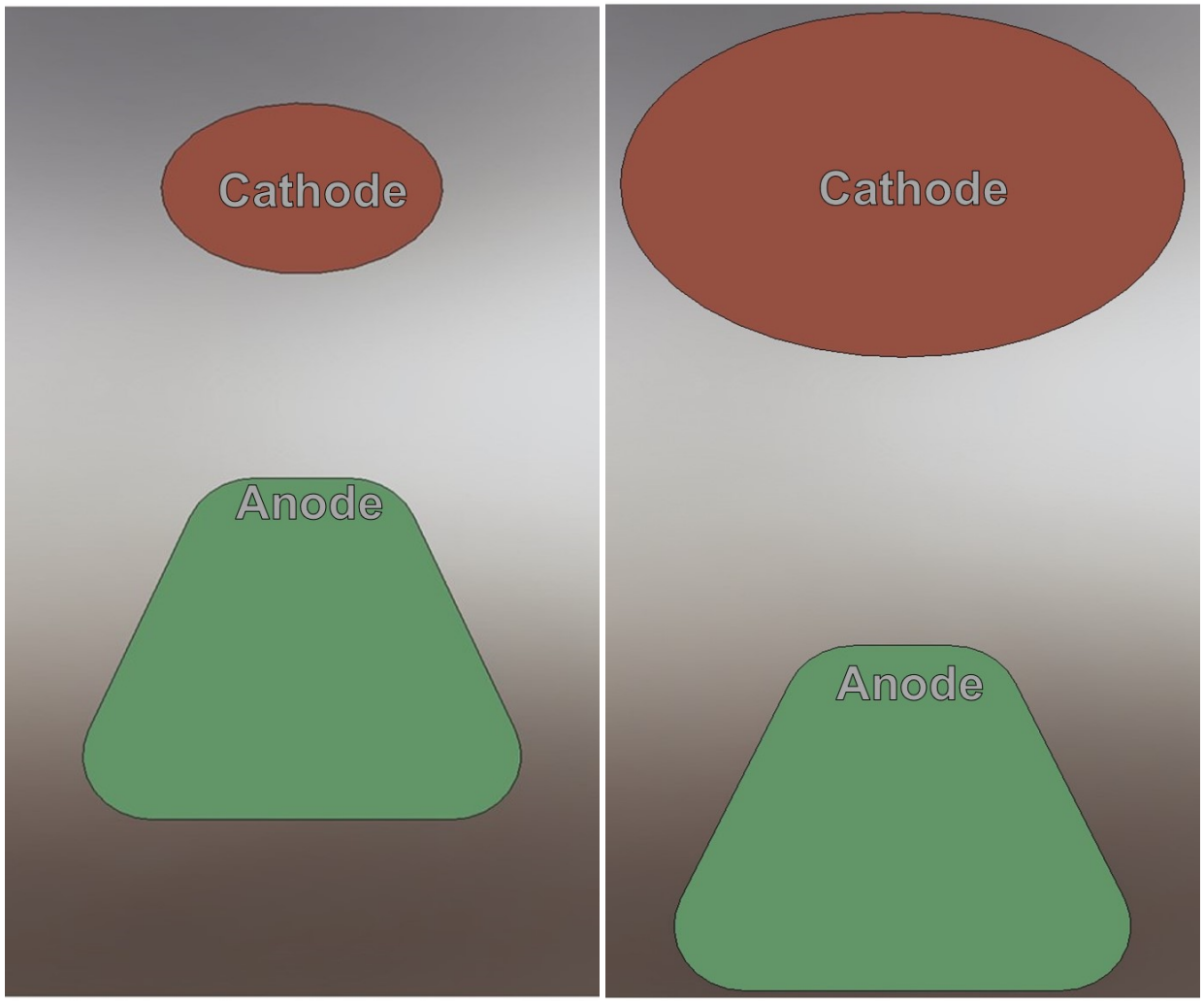

(a) Set #1 **(b) Set #2**

Figure 5.4. Cross sectional views of Mykonos' parallel plate plasma formation experimental hardware, where the cathode rod is red and anode rod is green. The geometries are (a) 1.50×1.00 mm cathode with 1.21 mm gap spacing, and (b) 3.00×2.00 mm cathode with 1.70 mm gap spacing. The anode rods all had a rounded edge isosceles trapezoid shape with a height of 2.00 mm, lower width of 2.00 mm, and upper width of 1.00 mm.

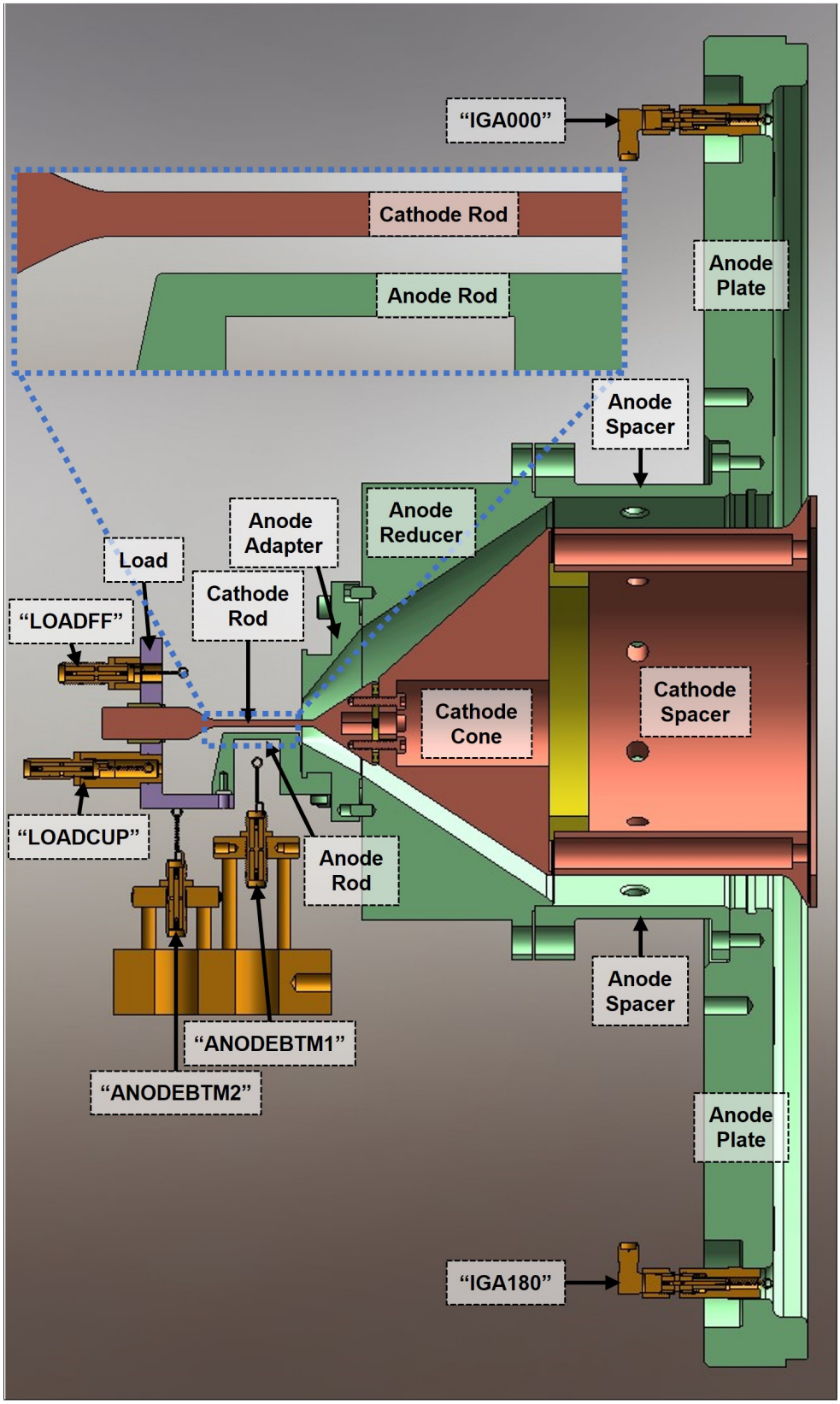

Figure 5.5. Right plane sectional view of the entire Mykonos parallel plate plasma formation hardware; color coded as (green) anode hardware, (red) cathode hardware, (purple) load hardware, (yellow) insulator material, and (orange) B-dot diagnostics. The cathode rod has a section length of 28.10 mm and the anode rod had a section length of 13.36 mm.

Extensive self-emission, Fig. (5.6), and shadowgraphy, Fig. (5.7), image data has been collected on this parallel plate hardware geometry for studies on MITL electrode surface cleaning techniques to mitigate current loss [37]–[39]. Though is it well understood that plasmas are forming with varying density gradients, no temporal density measurement has been made of them before this LDRD project.

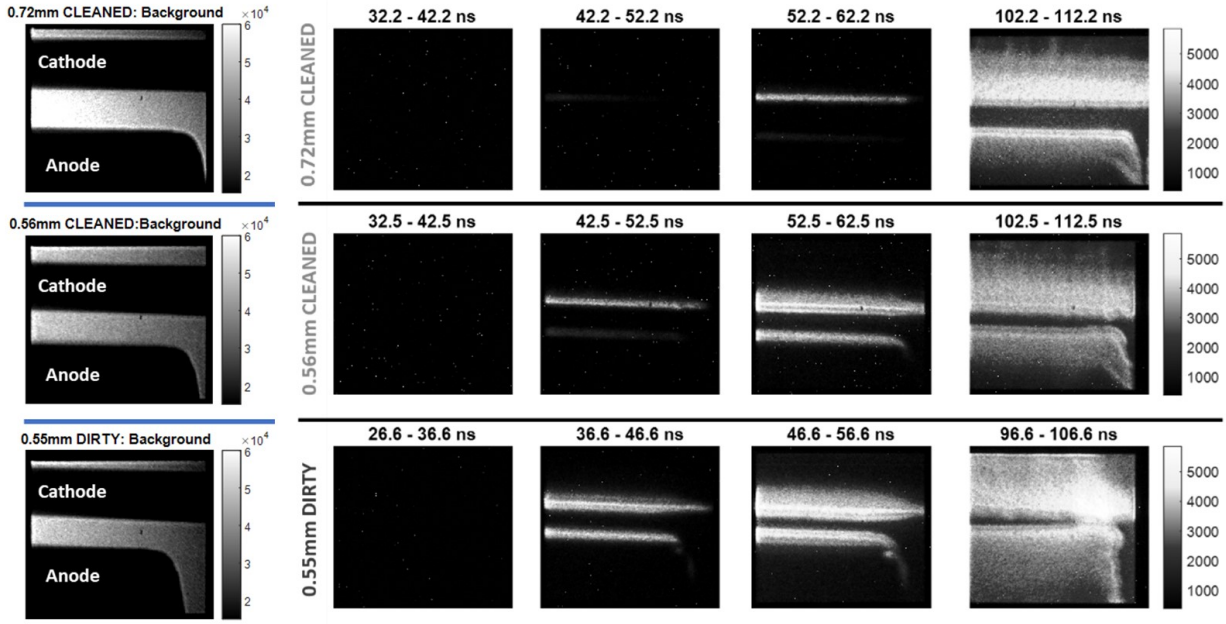

Figure 5.6. Self-emission images showing that plasma formation and apparent gap closure is delayed by in-situ plasma cleaning and larger gap spacing [39].

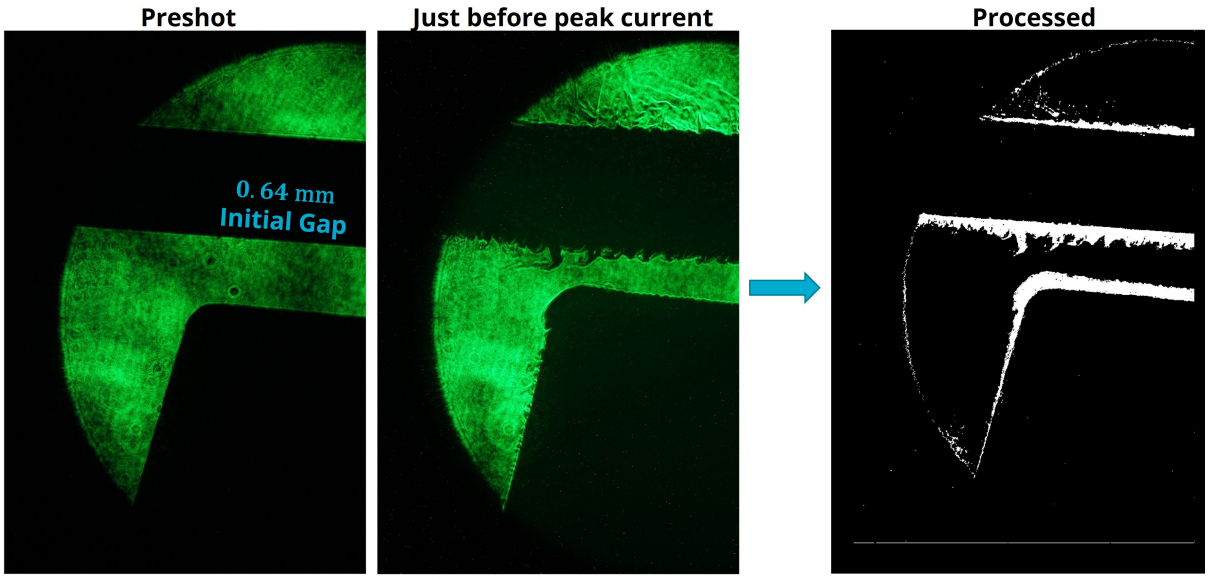

Figure 5.7. Shadowgraphy images showing a high density electrode plasma ($10^{19}\,\mathrm{cm}^{-3}\,/\,0.1\,\mathrm{mm}$) expanding into the parallel plate's A-K gap around the time of peak current delivery [40].

5.3. Necessary Colinear SHOP Interferometer Improvements for Mykonos

Fielding the colinear SHOP interferometer on Mykonos introduced challenges for the diagnostic to measure a plasma density that, compared to the HelCat plasma, was developing in significantly shorter time periods, had a reduction in shot-by-shot reproducibility, and was spatially much smaller. Two notable system improvements were required to allow the diagnostic to make electron density measurements within the Mykonos parallel plate A-K gap geometry, namely the inner chamber focusing optics and a detector sample rate upgrade.

5.3.1. Inner Chamber Focusing Optics

Along the UNM HelCat plasma probing path length the colinear SHOP interferometer's beam was collimated at a 2 mm diameter. A smaller probing beam diameter was required to pass the beam through the small Mykonos parallel plate A-K gaps. Ideally, the beam would be significantly smaller than the gap spacing to allow spatial variation in the probing location. The strategy implemented was to focus the probing beam through the A-K gap with the focal spot located in the gap. The use of achromatic doublet focusing lenses was necessary, since the lens would be focusing both the FH and SH wavelengths.

To reduce the spot size, the focusing lens' f-number was lowered. The f-number N is the ratio of the lens' focal length f to the initial beam diameter D. f = 150 mm lenses were mounted inside the 500 mm diameter vacuum chamber, and were protected from experiment-generated debris using debris shields. To further reduce the f-number, the collimated beam was increased from 2 mm to 8 mm. A ZEMAX ray traced optical diagram including the vacuum windows and debris shields for the 8 mm collimated beam diameter and $f = 150$ mm achromatic doublet lenses is shown in Fig. (5.8). To increase power transmission, all optics shown in Fig. (5.8) had an NIR-II anti-reflection optical coating providing $< 0.7\%$ reflectance per surface for 750-1550 nm wavelengths.

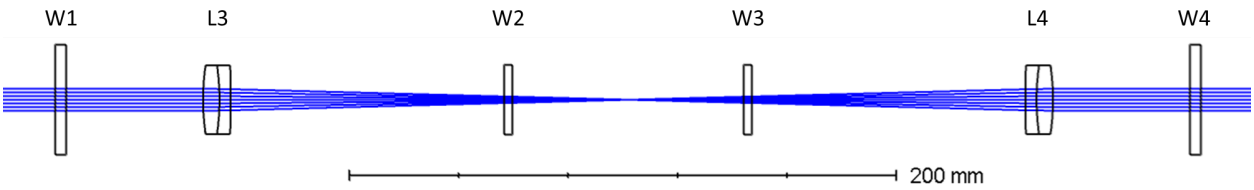

Figure 5.8. Optical layout used for ZEMAX calculations with blue ray traces showing beam propagation. Shown is the 40 mm diameter, 4 mm thick, λ/10, fused silica, vacuum window (W1 and W4); 25 mm diameter, 150 mm focusing length, achromatic doublet focusing lens (L3 and L4); 25.4 mm diameter, 3 mm thick, λ/10, fused silica, debris shield (W2 and W3).

For this optical layout, ZEMAX calculated a 1.084 mm difference in location of best focus between the FH and SH probing beams, and a minimum spot size (edge-to-edge diameter, assuming a uniform beam instead of Gaussian) of just 36 μm of the overlapped FH and SH beams. These values are the theoretical best achievable case for the achromatic doublet lenses

utilized. Transmitting the focusing beam through the debris shields had little effect on the location of best focus and minimum spot size. No direct measurement was made of the experimentally obtained probing beam's focusing parameters, but by visual inspection the minimum beam waist was ∼3-6 times larger than the optimum 36 μm.

5.3.2. Increasing Detector's Sample Rate

The detector used for UNM HelCat was a Si/PIN based 100 MHz bandwidth fixed gain balanced amplifier photodetector (ThorLabs PDB415A) [20]. This detector had the advantage of producing an output voltage proportional to the difference between the two optical input signals I_{+45} & I_{-45}, mentioned in Sec. (5.4.1), however the 100 MHz bandwidth was too slow for adequate detection of 1 ns density changes. The fastest balanced photodetector sensitive to 775 nm from ThorLabs had a bandwidth of only 350 MHz.

To increase the detector's bandwidth into the GHz range, the UNM detector was replaced by two Si based 2 GHz bandwidth photodetectors (ThorLabs DET025AFC), each individually detecting the I_{+45} & I_{-45} signals respectively. The two detectors' output signals were then subtracted via post-shot software analysis, instead of inherently in the detector's circuitry as was done before. This detector change didn't reduce the signal-to-noise ratio significantly.

5.3.3. Final Colinear SHOP Interferometer Design

With the inner chamber optical and detector improvements mentioned above, the final optical system layout was that shown in Fig. (5.9). The optical component parts list is also included below.

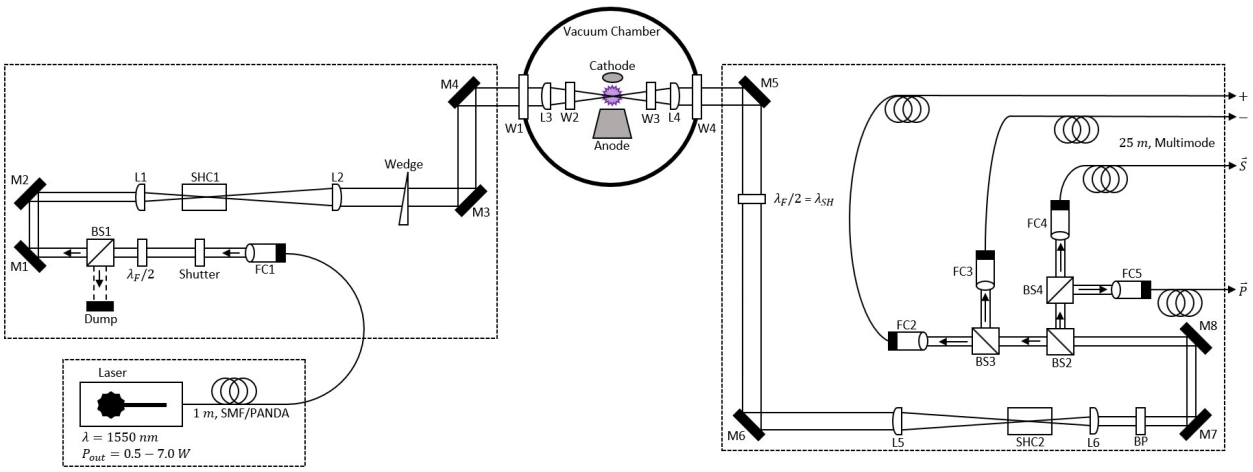

Figure 5.9. Diagram of the final colinear SHOP interferometer optical layout. Shown are the fiber triplet collimators (FC1 - FC5), shutter, FH half-wave-plates (λ_F/2), polarizing beamsplitter (BS1), f = 50 mm focusing lenses (L1 and L6), SH crystals (SHC1 and SHC2), f = 200 mm focusing lenses (L2 and L5), wedge, vacuum windows (W1 and W4), f = 150 mm focusing lenses (L3 and L4), debris shield windows (W2 and W3), 775 nm band-pass filter (BP), and alignment mirrors (M1 - M8).

Total Price	$ 49,508.46		
Component Label	**Part Number**	**Part Description**	**Part Price**
Laser	CEFL-KILO	Continuous Wave Erbium Fiber Laser	$ 25,000.00
FC1	TC12APC-1550	1550 nm, f=12.56 mm, NA=0.28, FC/APC Triplet Collimator	$ 552.03
	AD12F	SM1-Threaded Adapter for Ø12 mm, ≥0.35" (8.9 mm) Long Cylindrical Components	$ 34.36
	ST1XY-D	XY Translator with Differential Drives	$ 556.70
	RS06M	Ø24.5 mm Post Spacer, Thickness = 0.6 mm	$ 8.93
	RS02M	Ø24.0 mm Post Spacer, Thickness = 0.2 mm	$ 8.40
	RS3M	Ø25.0 mm Post Spacer, Thickness = 3 mm	$ 8.51
	PLS-P2	Ø1" Post for Polaris Mirror Mounts, One 8-32 Mounting Hole, L = 2.00"	$ 38.48
	POLARIS-CA1	Flexure Clamping Arm for Ø1" Posts, Non-Bridging, Stainless Steel, 1.30" Counterbored Slot, 1/4'	$ 88.77
Shutter	SH05	Optical Beam Shutter with 10' Long Cable, Ø1/2" Aperture, 8-32 Taps	$ 536.90
	KSC101	K-Cube Solenoid Controller (Power Supply Not Included)	$ 693.37
	KPS201	15 V, 2.66 A Power Supply Unit with 3.5 mm Jack Connector for One K- or T-Cube	$ 39.54
L_{F}/2	WPH05M-1550	Ø1/2" Zero-Order Half-Wave Plate, Ø1" Mount, 1550 nm	$ 497.30
BS1	CCM1-PBS25-1550	30 mm Cage-Cube-Mounted Polarizing Beamsplitter Cube, 1550 nm, 8-32 Tap	$ 385.49
	RS05M	Ø24.5 mm Post Spacer, Thickness = 0.5 mm	$ 8.93
	RS7M	Ø25.0 mm Post Spacer, Thickness = 7 mm	$ 9.26
	PLS-P238	Ø1" Post for Polaris Mirror Mounts, One 8-32 Mounting Hole, L = 2.38"	$ 39.83
	POLARIS-CA1	Flexure Clamping Arm for Ø1" Posts, Non-Bridging, Stainless Steel, 1.30" Counterbored Slot, 1/4'	$ 88.77
Dump	LB2	Beam Block, 1 - 12 µm, 80 W Max Avg. Power, Pulsed and CW, 8-32 Taps	$ 177.02
M1	UM10-45C	Ø1" Low GDD Ultrafast Mirror, 1400 nm - 1700 nm, 45° AOI	$ 285.60
	POLARIS-K1S4	Polaris® Ø1" Mirror Mount, 2 Hex Adjusters with Side Holes, Monolithic Optic Retention	$ 181.74
	RS01M	Ø24.0 mm Post Spacer, Thickness = 0.1 mm	$ 8.40
	RS1M	Ø25.0 mm Post Spacer, Thickness = 1 mm	$ 7.51
	PLS-P2	Ø1" Post for Polaris Mirror Mounts, One 8-32 Mounting Hole, L = 2.00"	$ 38.48
	POLARIS-CA1	Flexure Clamping Arm for Ø1" Posts, Non-Bridging, Stainless Steel, 1.30" Counterbored Slot, 1/4'	$ 88.77
M2	UM10-45C	Ø1" Low GDD Ultrafast Mirror, 1400 nm - 1700 nm, 45° AOI	$ 285.60
	POLARIS-K1S4	Polaris® Ø1" Mirror Mount, 2 Hex Adjusters with Side Holes, Monolithic Optic Retention	$ 181.74
	RS01M	Ø24.0 mm Post Spacer, Thickness = 0.1 mm	$ 8.40
	RS1M	Ø25.0 mm Post Spacer, Thickness = 1 mm	$ 7.51
	PLS-P2	Ø1" Post for Polaris Mirror Mounts, One 8-32 Mounting Hole, L = 2.00"	$ 38.48
	POLARIS-CA1	Flexure Clamping Arm for Ø1" Posts, Non-Bridging, Stainless Steel, 1.30" Counterbored Slot, 1/4'	$ 88.77
L1	AL2550J-C	Ø25.0 mm Diffraction-Limited N-BK7 Aspheric Lens, f = 50.0 mm, NA = 0.20, AR Coated: 1050 - 1	$ 342.54
	SM1L05	SM1 Lens Tube, 0.50" Thread Depth, One Retaining Ring Included	$ 13.62
	SM1Z	Z-Axis Translation Mount, 30 mm Cage Compatible	$ 215.88
	SM1L05	SM1 Lens Tube, 0.50" Thread Depth, One Retaining Ring Included	$ 13.62
	SM1D12CZ	SM1 Graduated Ring-Actuated Zero Aperture Iris Diaphragm, Ø12.0 mm Max Aperture	$ 133.93
	CP02B	30 mm Cage Mounting Bracket	$ 16.08
	PLS-P238	Ø1" Post for Polaris Mirror Mounts, One 8-32 Mounting Hole, L = 2.38"	$ 39.83
SHC1	1BKSL5P11936025020	PPMCLN 5 mol% Bulk Grading: Single 25L*2W*1T mm^3 SHG 19.36(um) Optically flat polished a	$ 800.00
	HP30-3x3	Heatpoint Oven for Nonlinear Crystals	$ 420.00
	CRM1L	Cage Rotation Mount for Ø1" Optics, Double Bored with Setscrew, 8-32 Tap	$ 106.86
	CP35	30 mm Cage Plate with Ø1" Double Bore, 8-32 Tap	$ 21.11
L2	#47-271	25mm Dia. x 200mm FL, NIR II Coated, Achromatic Lens	$ 127.00
	SM1L05	SM1 Lens Tube, 0.50" Thread Depth, One Retaining Ring Included	$ 13.62
	SM1Z	Z-Axis Translation Mount, 30 mm Cage Compatible	$ 215.88
	SM1L05	SM1 Lens Tube, 0.50" Thread Depth, One Retaining Ring Included	$ 13.62
	SM1D12CZ	SM1 Graduated Ring-Actuated Zero Aperture Iris Diaphragm, Ø12.0 mm Max Aperture	$ 133.93
	CP02B	30 mm Cage Mounting Bracket	$ 16.08
	PLS-P238	Ø1" Post for Polaris Mirror Mounts, One 8-32 Mounting Hole, L = 2.38"	$ 39.83
Wedge	WW42012-B	Ø2" UVFS Wedged Vacuum Window, AR Coating: 650 - 1050 nm	$ 188.40
	POLARIS-K2S2	Polaris® Low Drift Ø2" Mirror Mount, 2 Hex Adjusters	$ 285.34
	XR50P/M	50 mm Travel Linear Translation Stage, Side-Mounted Micrometer, M6 x 1.0 Taps	$ 827.80
	RS3M	Ø25.0 mm Post Spacer, Thickness = 3 mm	$ 8.51
	PLS-P1	Ø1" Post for Polaris Mirror Mounts, One 8-32 Mounting Hole, L = 1.00"	$ 34.66
	POLARIS-CA1	Flexure Clamping Arm for Ø1" Posts, Non-Bridging, Stainless Steel, 1.30" Counterbored Slot, 1/4'	$ 88.77
M3	#01-914-577	2" Dia. Protected Silver, λ/10 Flat Fused Silica	$ 297.50
	POLARIS-K2S2	Polaris® Low Drift Ø2" Mirror Mount, 2 Hex Adjusters	$ 285.34
	RS06M	Ø24.5 mm Post Spacer, Thickness = 0.6 mm	$ 8.93
	PLS-P2	Ø1" Post for Polaris Mirror Mounts, One 8-32 Mounting Hole, L = 2.00"	$ 38.48
	POLARIS-CA1	Flexure Clamping Arm for Ø1" Posts, Non-Bridging, Stainless Steel, 1.30" Counterbored Slot, 1/4'	$ 88.77

M4	#01-914-577	2" Dia. Protected Silver, λ/10 Flat Fused Silica	$ 297.50
	POLARIS-K2S2	Polaris® Low Drift Ø2" Mirror Mount, 2 Hex Adjusters	$ 285.34
	RS06M	Ø24.5 mm Post Spacer, Thickness = 0.6 mm	$ 8.93
	PLS-P2	Ø1" Post for Polaris Mirror Mounts, One 8-32 Mounting Hole, L = 2.00"	$ 38.48
	POLARIS-CA1	Flexure Clamping Arm for Ø1" Posts, Non-Bridging, Stainless Steel, 1.30" Counterbored Slot, 1/4'	$ 88.77
W1	#11-905	40mm Dia., 4mm Thick, NIR II Coated λ/10 Fused Silica Window	$ 215.00
	P107690	Demountable Viewport Conflat Flange (CF) 2.75, 1.19 in view, Uncoated Glass, Stainless Steel	$ 314.94
	P102241	Conflat Flange (CF) Zero Length Reducer, CF 6 inch through hole to 2-3/4 inch tapped hole, SS	$ 231.96
L3	#47-380	25mm Dia. x 150mm FL, NIR II Coated, Achromatic Lens	$ 127.00
	SM1L15	SM1 Lens Tube, 1.50" Thread Depth, One Retaining Ring Included	$ 16.98
	SM1TC	Clamp for SM1 Lens Tubes and C-Mount Extension Tubes	$ 49.20
W2	#15-421	25.4mm Dia., 3mm Thick, NIR II Coated λ/10 Fused Silica Window	$ 157.50
	SM1L20	SM1 Lens Tube, 2.00" Thread Depth, One Retaining Ring Included	$ 17.85
W3	#15-421	25.4mm Dia., 3mm Thick, NIR II Coated λ/10 Fused Silica Window	$ 157.50
	SM1L20	SM1 Lens Tube, 2.00" Thread Depth, One Retaining Ring Included	$ 17.85
L4	#47-380	25mm Dia. x 150mm FL, NIR II Coated, Achromatic Lens	$ 127.00
	SM1L15	SM1 Lens Tube, 1.50" Thread Depth, One Retaining Ring Included	$ 16.98
	SM1TC	Clamp for SM1 Lens Tubes and C-Mount Extension Tubes	$ 49.20
W4	#11-905	40mm Dia., 4mm Thick, NIR II Coated λ/10 Fused Silica Window	$ 215.00
	P107690	Demountable Viewport Conflat Flange (CF) 2.75, 1.19 in view, Uncoated Glass, Stainless Steel	$ 314.94
	P102241	Conflat Flange (CF) Zero Length Reducer, CF 6 inch through hole to 2-3/4 inch tapped hole, SS	$ 231.96
M5	#01-914-577	2" Dia. Protected Silver, λ/10 Flat Fused Silica	$ 297.50
	POLARIS-K2S2	Polaris® Low Drift Ø2" Mirror Mount, 2 Hex Adjusters	$ 285.34
	RS06M	Ø24.5 mm Post Spacer, Thickness = 0.6 mm	$ 8.93
	PLS-P2	Ø1" Post for Polaris Mirror Mounts, One 8-32 Mounting Hole, L = 2.00"	$ 38.48
	POLARIS-CA1	Flexure Clamping Arm for Ø1" Posts, Non-Bridging, Stainless Steel, 1.30" Counterbored Slot, 1/4'	$ 88.77
L_{F}/2 = L_{SH}	DFH-100-775/1550	1550 nm half wave plate, 775 nm full wave plate	$ 1,248.00
	CRM1L	Cage Rotation Mount for Ø1" Optics, Double Bored with Setscrew, 8-32 Tap	$ 106.86
M6	#01-914-577	2" Dia. Protected Silver, λ/10 Flat Fused Silica	$ 297.50
	POLARIS-K2S2	Polaris® Low Drift Ø2" Mirror Mount, 2 Hex Adjusters	$ 285.34
	RS06M	Ø24.5 mm Post Spacer, Thickness = 0.6 mm	$ 8.93
	PLS-P2	Ø1" Post for Polaris Mirror Mounts, One 8-32 Mounting Hole, L = 2.00"	$ 38.48
	POLARIS-CA1	Flexure Clamping Arm for Ø1" Posts, Non-Bridging, Stainless Steel, 1.30" Counterbored Slot, 1/4'	$ 88.77
L5	#47-271	25mm Dia. x 200mm FL, NIR II Coated, Achromatic Lens	$ 127.00
	SM1L05	SM1 Lens Tube, 0.50" Thread Depth, One Retaining Ring Included	$ 13.62
	SM1Z	Z-Axis Translation Mount, 30 mm Cage Compatible	$ 215.88
	SM1L05	SM1 Lens Tube, 0.50" Thread Depth, One Retaining Ring Included	$ 13.62
	SM1D12CZ	SM1 Graduated Ring-Actuated Zero Aperture Iris Diaphragm, Ø12.0 mm Max Aperture	$ 133.93
	CP02B	30 mm Cage Mounting Bracket	$ 16.08
	PLS-P238	Ø1" Post for Polaris Mirror Mounts, One 8-32 Mounting Hole, L = 2.38"	$ 39.83
SHC2	1BKSL5P11936025020	PPMCLN 5 mol% Bulk Grading: Single 25L*2W*1T mm^3 SHG 19.36(um) Optically flat polished a	$ 800.00
	HP30-3x3	Heatpoint Oven for Nonlinear Crystals	$ 420.00
	CRM1L	Cage Rotation Mount for Ø1" Optics, Double Bored with Setscrew, 8-32 Tap	$ 106.86
	CP35	30 mm Cage Plate with Ø1" Double Bore, 8-32 Tap	$ 21.11
L6	#45-803	25mm Dia. x 50mm FL, NIR II Coated, Achromatic Lens	$ 127.00
	SM1L05	SM1 Lens Tube, 0.50" Thread Depth, One Retaining Ring Included	$ 13.62
	SM1Z	Z-Axis Translation Mount, 30 mm Cage Compatible	$ 215.88
	SM1L05	SM1 Lens Tube, 0.50" Thread Depth, One Retaining Ring Included	$ 13.62
	SM1D12CZ	SM1 Graduated Ring-Actuated Zero Aperture Iris Diaphragm, Ø12.0 mm Max Aperture	$ 133.93
	CP02B	30 mm Cage Mounting Bracket	$ 16.08
	PLS-P238	Ø1" Post for Polaris Mirror Mounts, One 8-32 Mounting Hole, L = 2.38"	$ 39.83
BP	#87-794	775nm CWL, 25mm Dia. Hard Coated OD 4.0 25nm Bandpass Filter	$ 255.00
	SM1L03	SM1 Lens Tube, 0.30" Thread Depth, One Retaining Ring Included	$ 13.15
	#89-573	1150nm 25mm Diameter, OD 4.0 Shortpass Filter	$ 270.00
	SM1L03	SM1 Lens Tube, 0.30" Thread Depth, One Retaining Ring Included	$ 13.15
	CP360R	Pivoting, Quick-Release, Ø1" Optic Mount for 30 mm Cage System	$ 109.20
	FW1A	Filter Wheel Station for Ø1" Filters, One Wheel, 6 Filter Capacity	$ 177.02
M7	UM10-45A	Ø1" Low-GDD Ultrafast Mirror, 700 nm - 930 nm, 45° AOI	$ 244.65
	POLARIS-K1S4	Polaris® Ø1" Mirror Mount, 2 Hex Adjusters with Side Holes, Monolithic Optic Retention	$ 181.74
	RS01M	Ø24.0 mm Post Spacer, Thickness = 0.1 mm	$ 8.40
	RS1M	Ø25.0 mm Post Spacer, Thickness = 1 mm	$ 7.51
	PLS-P2	Ø1" Post for Polaris Mirror Mounts, One 8-32 Mounting Hole, L = 2.00"	$ 38.48
	POLARIS-CA1	Flexure Clamping Arm for Ø1" Posts, Non-Bridging, Stainless Steel, 1.30" Counterbored Slot, 1/4'	$ 88.77

M8	UM10-45A	Ø1" Low-GDD Ultrafast Mirror, 700 nm - 930 nm, 45° AOI	$ 244.65
	POLARIS-K1S4	Polaris® Ø1" Mirror Mount, 2 Hex Adjusters with Side Holes, Monolithic Optic Retention	$ 181.74
	RS01M	Ø24.0 mm Post Spacer, Thickness = 0.1 mm	$ 8.40
	RS1M	Ø25.0 mm Post Spacer, Thickness = 1 mm	$ 7.51
	PLS-P2	Ø1" Post for Polaris Mirror Mounts, One 8-32 Mounting Hole, L = 2.00"	$ 38.48
	POLARIS-CA1	Flexure Clamping Arm for Ø1" Posts, Non-Bridging, Stainless Steel, 1.30" Counterbored Slot, 1/4'	$ 88.77
BS2	CCM1-BS014	30 mm Cage Cube-Mounted Non-Polarizing Beamsplitter, 700 - 1100 nm, 8-32 Tap	$ 330.75
	RS05M	Ø24.5 mm Post Spacer, Thickness = 0.5 mm	$ 8.93
	RS7M	Ø25.0 mm Post Spacer, Thickness = 7 mm	$ 9.26
	PLS-P238	Ø1" Post for Polaris Mirror Mounts, One 8-32 Mounting Hole, L = 2.38"	$ 39.83
	POLARIS-CA1	Flexure Clamping Arm for Ø1" Posts, Non-Bridging, Stainless Steel, 1.30" Counterbored Slot, 1/4'	$ 88.77
BS3	CCM1-PBS25-780	30 mm Cage-Cube-Mounted Polarizing Beamsplitter Cube, 780 nm, 8-32 Tap	$ 385.49
	ER05-P4	Cage Assembly Rod, 1/2" Long, Ø6 mm, 4 Pack	$ 20.76
	ER05-P4	Cage Assembly Rod, 1/2" Long, Ø6 mm, 4 Pack	$ 20.76
	CPU1	30 mm Rotating Cage Segment Plate, Two SM1RR Retaining Rings Included, Imperial	$ 178.19
FC2	TC12FC-780	780 nm, f=12.19 mm, NA=0.28, FC/PC Triplet Collimator	$ 478.66
	AD12F	SM1-Threaded Adapter for Ø12 mm, ≥0.35" (8.9 mm) Long Cylindrical Components	$ 34.36
	CXY1	30 mm Cage System, XY Translating Lens Mount for Ø1" Optics	$ 201.47
	ER1-P4	Cage Assembly Rod, 1" Long, Ø6 mm, 4 Pack	$ 20.76
FC3	TC12FC-780	780 nm, f=12.19 mm, NA=0.28, FC/PC Triplet Collimator	$ 478.66
	AD12F	SM1-Threaded Adapter for Ø12 mm, ≥0.35" (8.9 mm) Long Cylindrical Components	$ 34.36
	CXY1	30 mm Cage System, XY Translating Lens Mount for Ø1" Optics	$ 201.47
	ER1-P4	Cage Assembly Rod, 1" Long, Ø6 mm, 4 Pack	$ 20.76
BS4	CCM1-PBS25-780	30 mm Cage-Cube-Mounted Polarizing Beamsplitter Cube, 780 nm, 8-32 Tap	$ 385.49
	CM1-CC	Cage Cube Connector for Compact 30 mm Cage Cubes	$ 52.42
FC4	TC12FC-780	780 nm, f=12.19 mm, NA=0.28, FC/PC Triplet Collimator	$ 478.66
	AD12F	SM1-Threaded Adapter for Ø12 mm, ≥0.35" (8.9 mm) Long Cylindrical Components	$ 34.36
	CXY1	30 mm Cage System, XY Translating Lens Mount for Ø1" Optics	$ 201.47
	ER1-P4	Cage Assembly Rod, 1" Long, Ø6 mm, 4 Pack	$ 20.76
FC5	TC12FC-780	780 nm, f=12.19 mm, NA=0.28, FC/PC Triplet Collimator	$ 478.66
	AD12F	SM1-Threaded Adapter for Ø12 mm, ≥0.35" (8.9 mm) Long Cylindrical Components	$ 34.36
	CXY1	30 mm Cage System, XY Translating Lens Mount for Ø1" Optics	$ 201.47
	ER1-P4	Cage Assembly Rod, 1" Long, Ø6 mm, 4 Pack	$ 20.76

5.4. Mykonos Interferometer Data & Comparison to Simulations

This section discusses the colinear SHOP interferometer's data collected and calculated areal density measurements made on both hardware sets listed in Fig (5.4). It also compares the interferometer's data to CHICAGO and ALEGRA simulation results.

5.4.1. Data Analysis

For reference, shot #014992's pre-shot calibration and I_{+45} and I_{-45} raw signal data are shown in Fig. (5.10). The four black traces in the shot data correspond to the four B-dot probes' measured machine current.

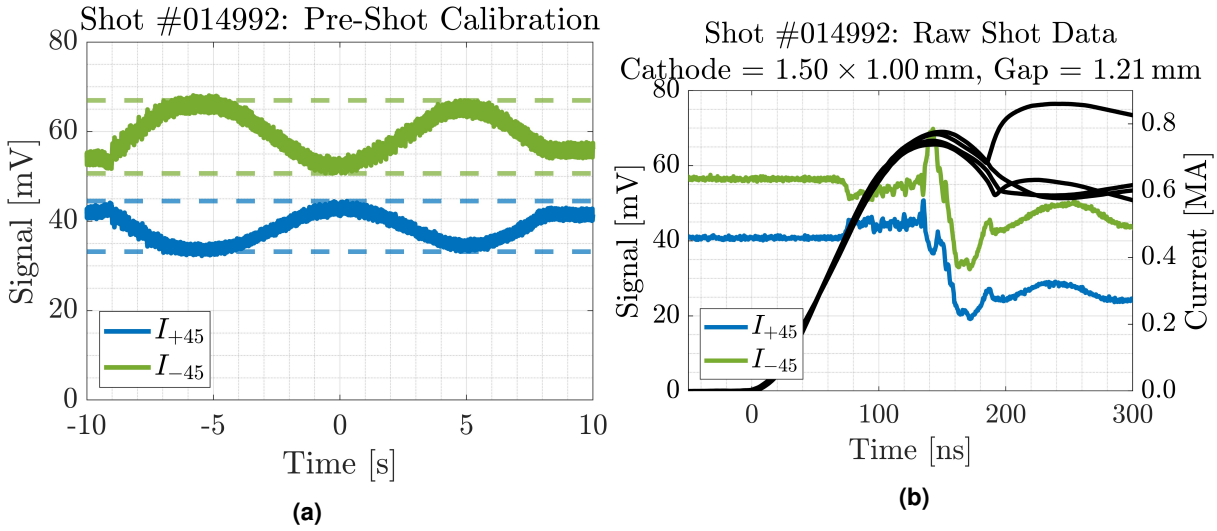

Figure 5.10. The I_{+45} and I_{-45} raw signal traces for shot #014992's (a) pre-shot calibration and (b) raw shot data. The four black traces in (b) correspond to the four IGA B-dot probes' measured machine current.

The pre-shot sweep allows for calibration of the signals' amplitude A and offset DC, so that we can accurately track the phase change $\Delta\Phi$ during the Mykonos shot calculated from the signal voltage V via

$$V = A\sin(\Delta\Phi + \phi_0) + DC\,. \tag{5.1}$$

This phase change $\Delta\Phi$ can then be used to calculate the areal density $\langle n_e L\rangle$ via Eq. (3.12). However, the signal voltage can change not only because of a change in phase via plasma density changes. The signal voltage can also change by changes in amplitude and offset values via self-emission (leading to an increase in signal voltage) or absorption or refraction (leading to a decrease in signal voltage), both of which would render the pre-shot calibration sweep invalid. The change in power levels during Mykonos shot #14992 can be calculated by equalizing the two I_{+45} and I_{-45} shot signals' initial amplitudes and offsets then plotting the average of the two adjusted signals, shown in Fig. (5.11).

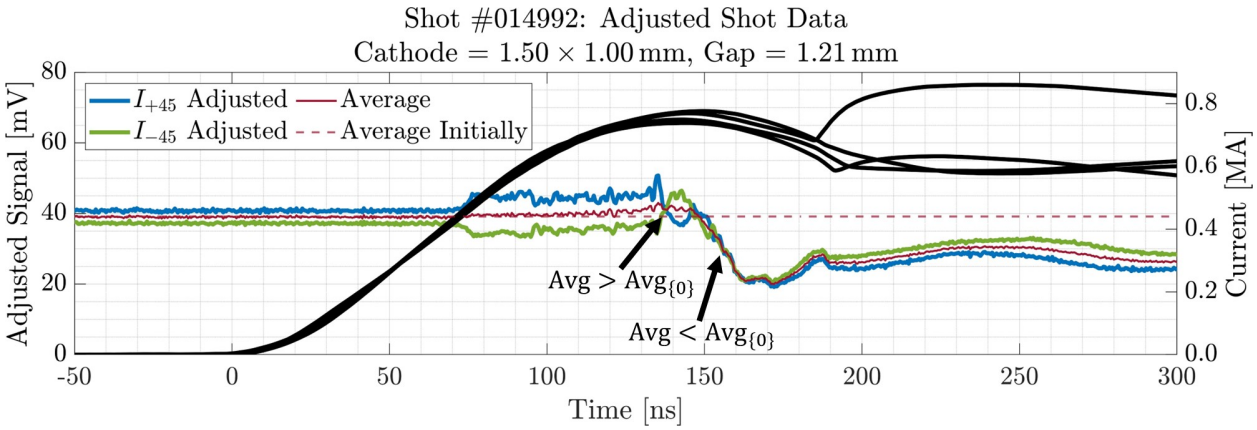

Figure 5.11. Plot of the shot #014992 initial amplitude and offset adjusted I_{+45} and I_{-45} signals as well as their average and initial average signal. The average signal increases above the initial average signal between 75-148 ns, and decreases below the initial average signal for the remainder of the shot.

If the adjusted signals didn't encounter a change in amplitude and offset then they would continue to be out of phase with respect to each other throughout the shot, and the their average signal would stay constant for all time. To calculate the phase using the pre-shot calibration data, the adjusted shot data occurring after an average signal fluctuation of $> 3.5\%$ from the initial average signal was rejected and the I_{+45} and I_{-45} signal adjusted data was normalized to the average signal data, as shown in Fig. (5.12). Also, the same has been done with their respective calibration amplitude bounds.

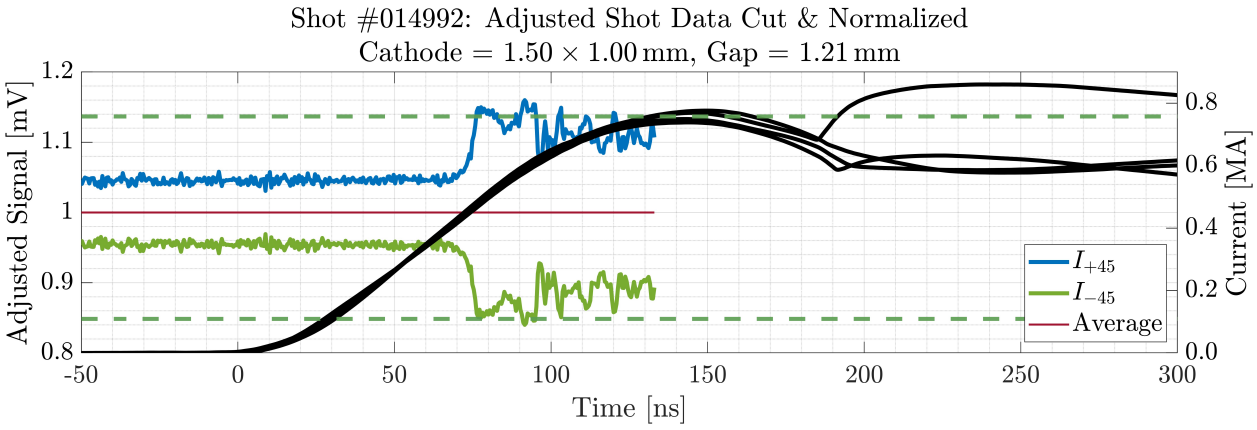

Figure 5.12. Plot of the shot #014992 adjusted I_{+45} and I_{-45} signal data normalized to the temporal power level and cutoff once power fluctuated by 3.5%.

Now that there are two adjusted I_{+45} and I_{-45} signals that are exclusively out of phase, the difference of the two signals is taken to remove the offset value via Eq. (3.3), shown in Fig. (5.13). Completing this subtraction step via post-shot software analysis caries no detection sensitivity advantage since the phase data is inherent within these power adjusted I_{+45} and I_{-45} signals. However, if differentiating was completed inherently withing the detector circuit (like what was done with the previously used fixed gain balanced amplifier photodetector), then gain

could be applied to solely the amplitude and not the offset and potentially increase the signal-to-noise ratio. If detection is made solely on the fixed gain balanced amplifier photodetector's output I_{Diff} signal, any potential variation in power from self-emission or absorption is inherently calibrated out since it affects both the I_{+45} and I_{-45} input signals equally. The differentiating process is completed here to help correlate the previously utilized I_{Diff} signal to the I_{+45} and I_{-45} adjusted signals.

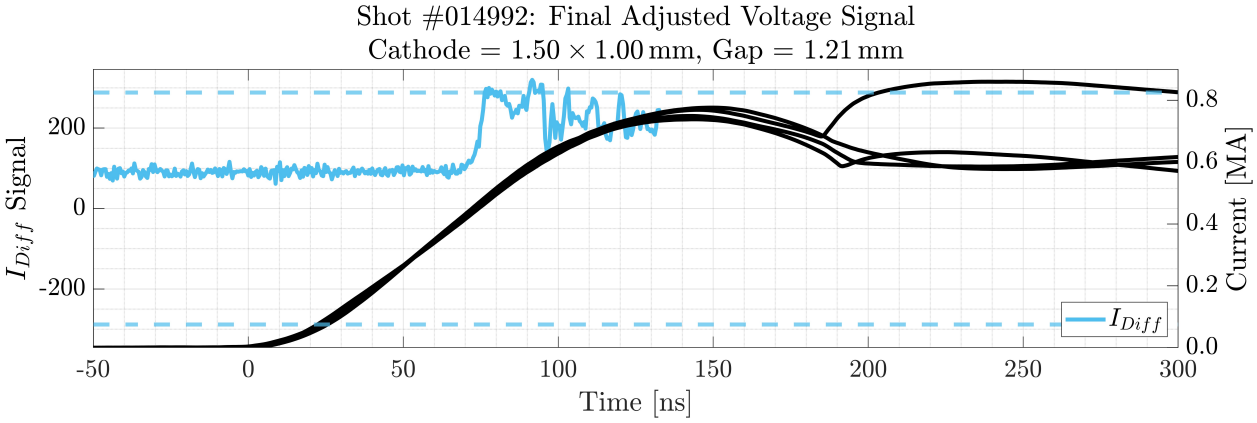

Figure 5.13. Plot of the shot #014992 I_{Diff} signal calculated from the I_{+45} and I_{-45} signal data shown in Fig. (5.12) via Eq. (3.3).

From the plotted I_{diff} signal data, Eq. (5.1) can be used to calculate the temporal phase change shown in Fig. (5.14). For the purposes of this analysis, any data points extending outside of the amplitude bounds were excluded under the assumption that signal noise was the cause. This is done since is is physically unrealizable to calculate a real phase from a signal if the signal extends above or below the defined amplitude.

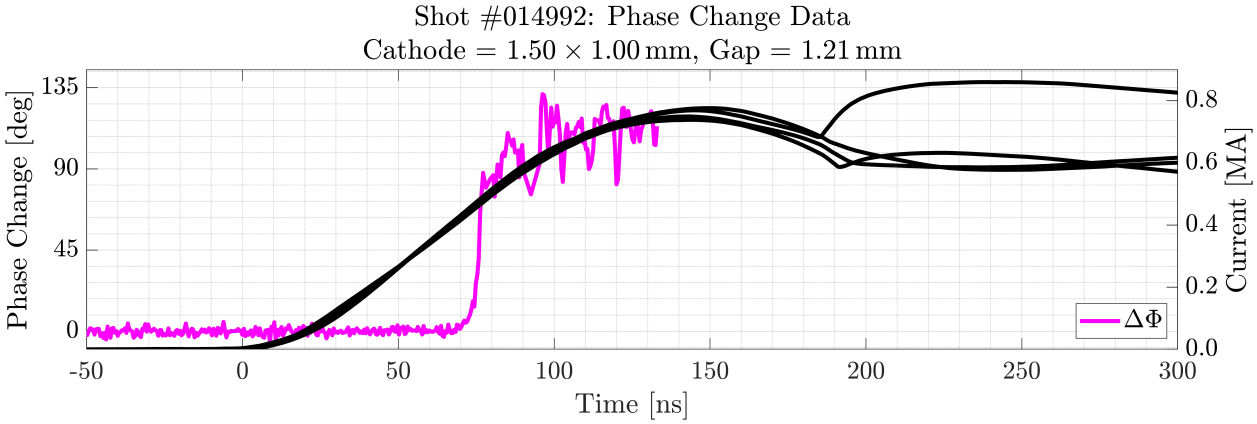

Figure 5.14. Plot of the shot #014992 calculated temporal phase change.

The temporal phase data from Fig. (5.14) is then used to calculate the temporal areal density via Eq. (3.12). The areal density data for Mykonos shot #014992 is discussed further in the next section.

5.4.2. *Hardware Set #1*

Hardware set #1 represents the 1.50×1.00 mm cathode and 1.21 mm gap spacing. The areal density measurement collected on Mykonos shot #014992 was obtained while probing just off of the cathode's inner surface, as shown in Fig. (5.15a). Again, the four black traces in the shot data correspond to the four B-dot probes' measured machine current.

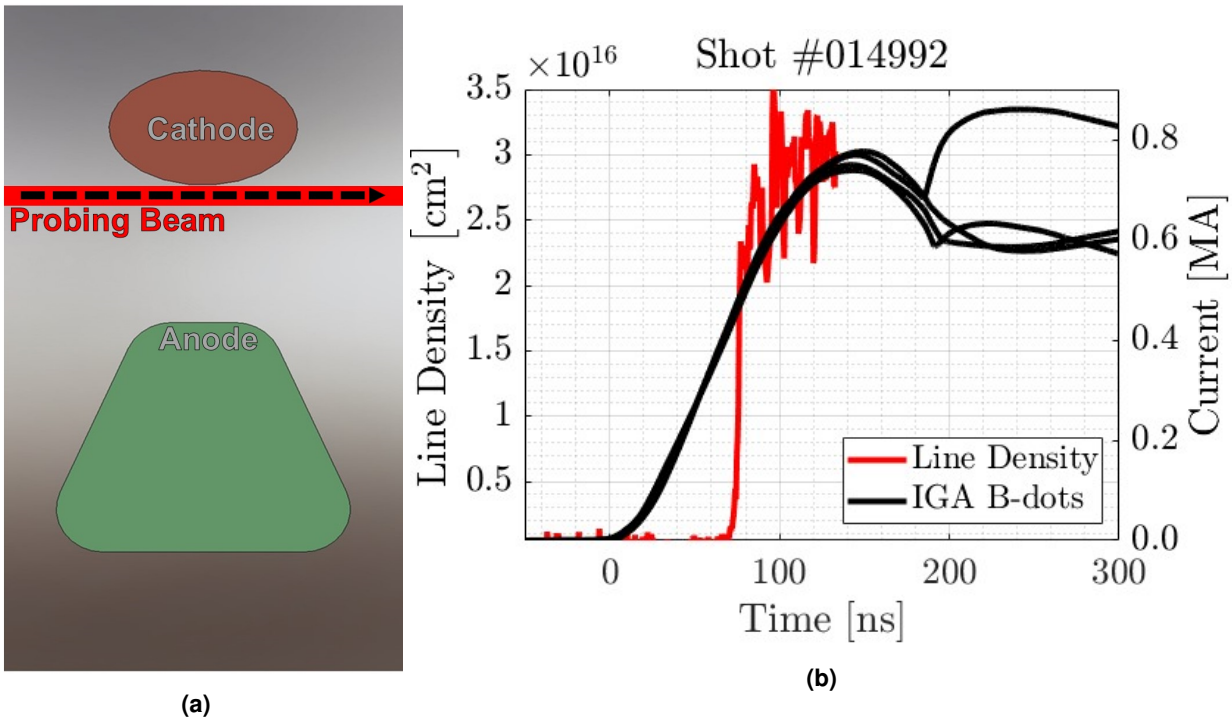

Figure 5.15. On the left is (a) the cross sectional view of A-K hardware set #1 with a representative colinear SHOP interferometer probing beam size and location that was used to collect (b) data during shot #014992.

Enlarging Fig. (5.15b) for the region of interest, we see a 7 ns period of roughly exponential areal density increase (from 70-77 ns), followed by a noisy or turbulent 56 ns roughly linear increase (from 77-133 ns), shown in Fig. (5.16).

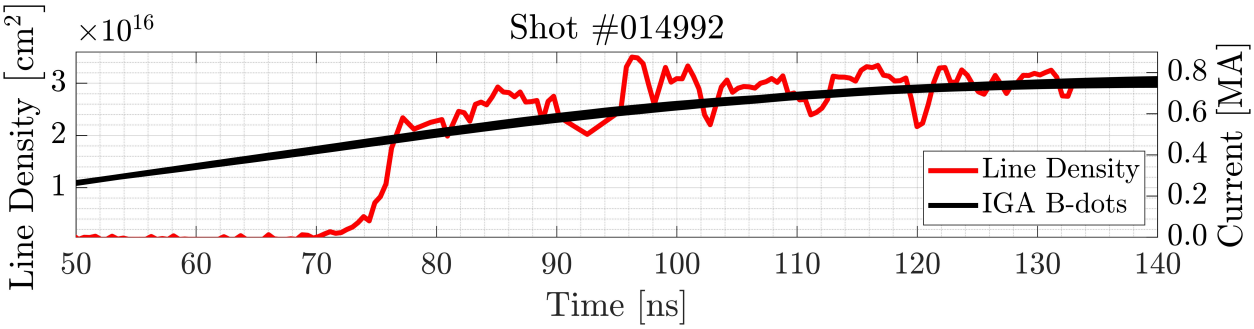

Figure 5.16. Enlarged view of Fig. (5.15b), highlighting the 7 ns period of roughly exponential areal density increase (from 70-77 ns), followed by a noisy or turbulent 56 ns roughly linear increase (from 77-133 ns).

At 133 ns, the signal power levels fluctuated by > 3.5%, rendering the pre-shot calibration sweep data invalid for further analysis. In the data shown for Shot #014992, the power levels increased by 3.5% at 133 ns, likely due to the plasma's self-emission at the 25 nm FWHM line-filtered 775 nm wavelength. The signal data did not decrease power levels by 3.5% from the calibration levels until $\sim$ 150 ns, marking the beginning of the high density electrode plasma's significant expansion across the interferometer's probing beam, mentioned in Sec. (5.2) and shown in the shadowgraphy image of Fig. (5.7).

To contribute to the understanding of how the inner A-K gap plasmas form and behave, the CHICAGO three-dimensional fully electromagnetic Particle-In-Cell (PIC) code was used to model the hardware, shown in Fig. (5.17). These simulations are still ongoing and are being conducted by David Rose from Voss Scientific.

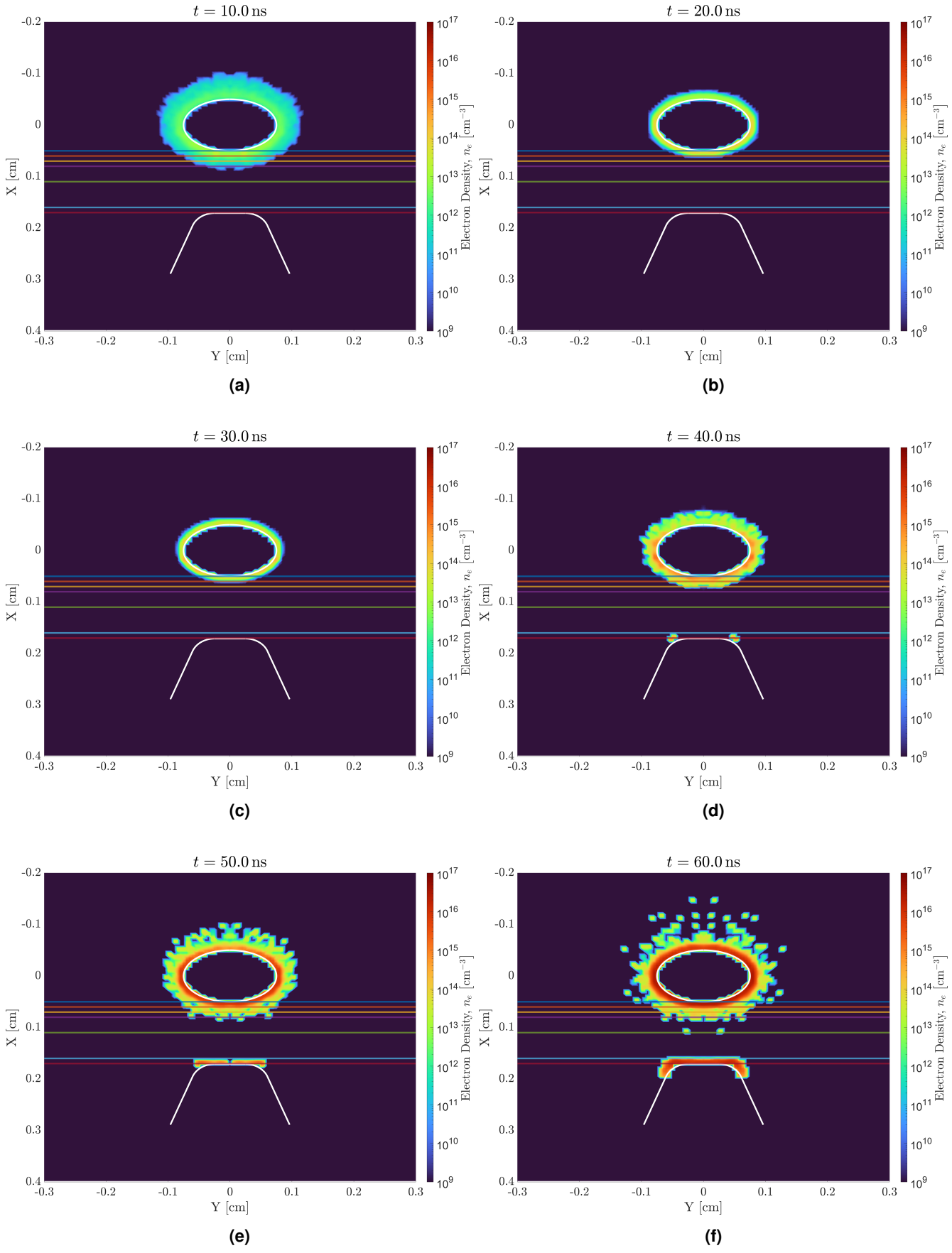

Figure 5.17. Several heat map images showing the CHICAGO simulation's spatially resolved electron densities [cm^{-3}] of the 1.50×1.00 mm cathode with a 1.21 mm gap spacing hardware geometry. Shown are images corresponding to time stamps of (a) 10 ns, (b) 20 ns, (c) 30 ns, (d) 40 ns, (e) 50 ns, and (f) 60 ns during the Mykonos current pulse.

Line-averaged electron density $\langle n_e L \rangle$ can be calculated from these simulations by summing the areal densities of a given point $n_{e,i}\,(y_{i+1} - y_i)$ for all y points along a set x lineout as

$$\langle n_e L \rangle = \sum_{i=1}^{i=N_y-1} n_{e,i}\,(y_{i+1} - y_i)\,. \tag{5.2}$$

Various temporal x lineout areal density calculations from the 1.50×1.00 mm cathode with a 1.21 mm gap spacing hardware geometry CHICAGO simulation are shown in Fig. (5.18). The variable weight macro particles on the edge surface between vacuum and plasma lead to statistical noise, so a 2 ns (20 point) moving average was taken.

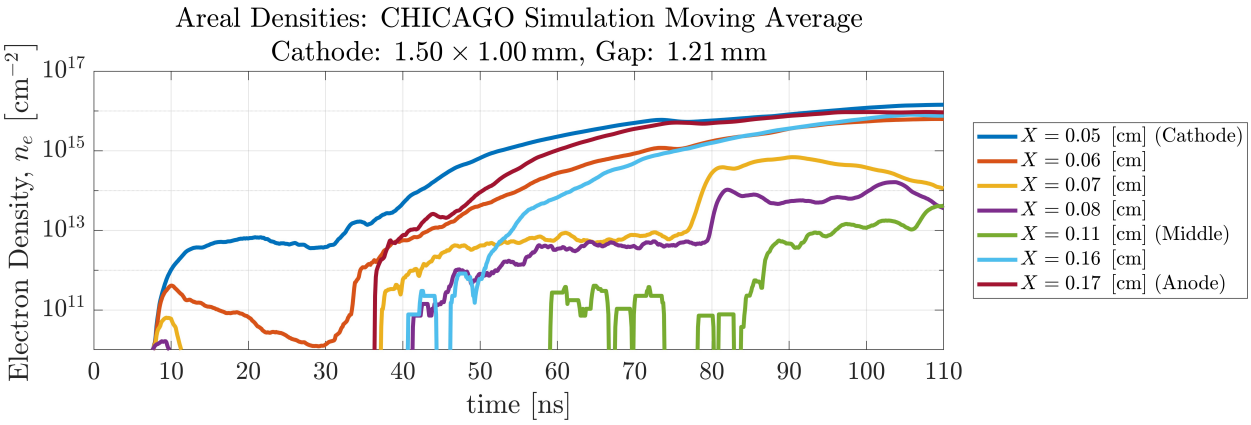

Figure 5.18. 2 ns moving averages of the various temporal x lineout areal density calculations from the 1.50×1.00 mm cathode with a 1.21 mm gap spacing hardware geometry CHICAGO simulation.

Comparison of the colinear SHOP interferometer's areal density measurement, Fig. (5.16), to the CHICAGO simulation areal densities along similar probing paths, Fig. (5.18), is shown in Fig. (5.19). The CHICAGO simulations for this hardware geometry are ongoing, but as of now have run out to 110 ns. The colinear SHOP interferometer's signal data did not begin to exceed the noise threshold until 70.7 ns and the signal's power level fluctuated by >3.5% at 133 ns.

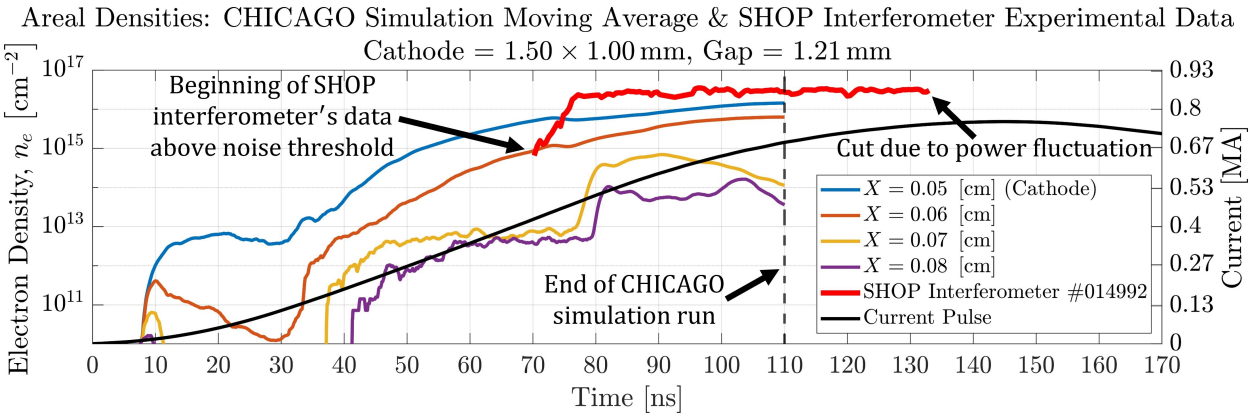

Figure 5.19. Plotted are the areal densities from three calculated lineouts from the CHICAGO simulation that are located close to the cathode surface, as well as the experimentally obtained Mykonos shot #014992 areal density data also collected close to the cathode surface.

The $x = 0.06\,\text{cm}$ (100 μm away from the cathode surface) line-averaged density from CHICAGO intersects the beginning of the experimental colinear SHOP interferometer data collected from Mykonos shot #014992 when probing just under the cathode surface. This is expected, since we stated in Sec. (5.3.1) that our Gaussian probing beam likely had a 100 - 200 μm diameter, and thus the beam's peak intensity would be located 50 - 100 μm off of the cathode surface.

However, the interferometer data shows a faster density increase between 70 - 77 ns followed by a sharp roll-off. This density trajectory matches more closely to that of CHICAGO's $x = 0.07\,\text{cm}$ and $x = 0.08\,\text{cm}$ (200 μm and 300 μm away from the cathode surface respectively) line-averaged density traces. This discrepancy could be caused by the effects of hydrodynamic electrode gap closure, which the CHICAGO simulation doesn't include.

To further understand the electrode behavior, ALEGRA shock hydrodynamics and multiphysics simulations were conducted. Shown in Fig. (5.20) is the electrode surface temperatures along the center line (where the A-K electrodes have the smallest gap spacing).

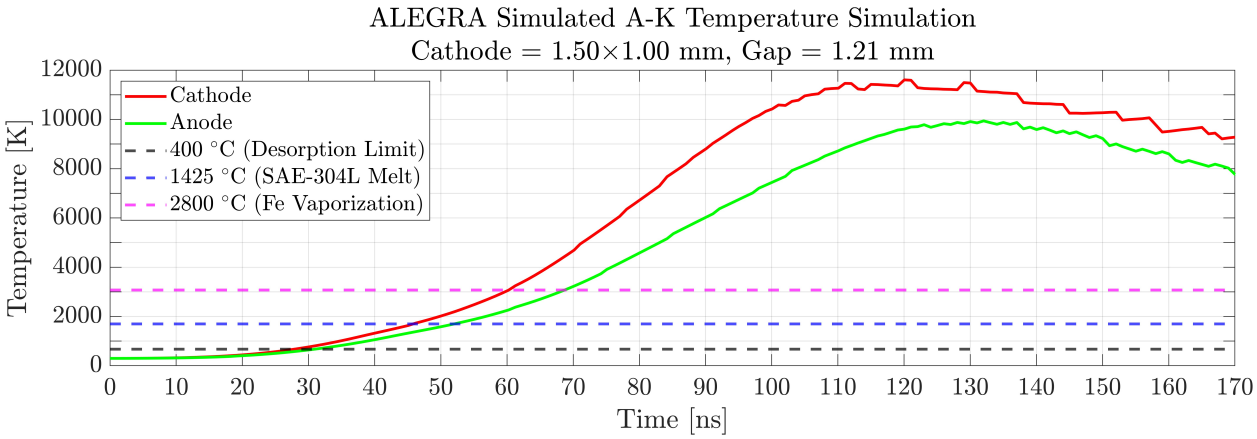

Figure 5.20. ALEGRA simulation results for the anode and cathode surface temperatures along the center line (where the A-K gap spacing is smallest).

The simulation results from in Fig. (5.20) show that the electrodes exceed the 400°C desorption threshold at 31 ns and 28 ns for the anode and cathode respectively, and they each exceed the melt temperature of SAE-304L at 52 ns and 46 ns respectively. During the period before the electrodes reach the 400°C desorption threshold (0 - 29 ns), the CHIGACO simulations lineouts see a reduction in areal density phase. This effect is likely due to a lack of substantial plasma formation but an increase in current flow and hence an increase in plasma confinement. After the electrodes reach an excess of 400°C (> 29 ns), desorption occurs and substantial plasma formation takes place leading to the increase in plasma density seen in the CHICAGO simulation lineouts.

The ALEGRA simulations were also able to provide data on electrode movement (the "gap closure") sourced by internal shocks, shown in Fig. (5.21). The simulation results in Fig. (5.21) show that the gap spacing reduces by less than 1% before 60ns. Therefore, it's likely that the CHICAGO simulations up to this time, which don't factor electrode movement, have little error from electrode movement. However, the ALEGRA simulation shows that there is 5% gap closure by 99 ns and 10% gap closure by 115 ns.

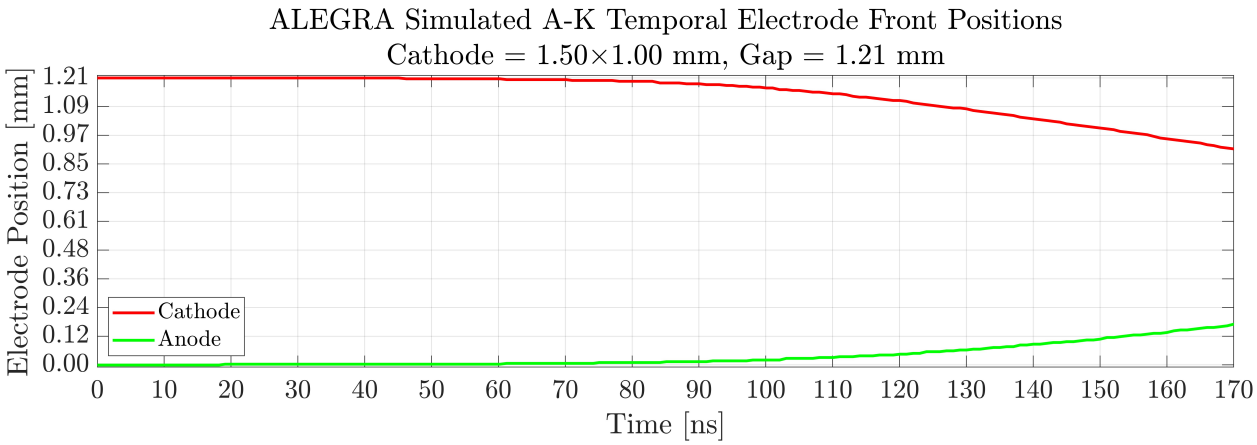

Figure 5.21. ALEGRA simulation results for the anode and cathode surface fronts along the center line (where the A-K gap spacing is smallest). This shows the high density material moving inward and reducing the gap spacing.

Fig. (5.21) also shows a 151.7 μm cathode front expansion into the gap at 135 ns, which is when the average power from shot #014992 begun to decrease. A 211.4 μm cathode front expansion is seen at 150 ns, which is when the average power from shot #014992 reduced below 3.5% of the initial average power. A 302.9 μm cathode front expansion is seen at 171 ns, which is when the shot #014992 signal data experienced it's lowest average power level. The electrode expansion at these three moments helps to corroborate that the colinear SHOP interferometer's beam diameter was likely on the order of 50 - 300 μm, since it would be expected that the expanding electrode material would block the probing beam's optical path and lower the detected power.

The electrode material's movement into the A-K gap would also have the the effect of driving the surface plasma further into the gap. It would then be expected that the colinear SHOP interferometer would measure a higher areal density plasma as the electrodes move into the gap, effectively changing the interferometer's probing beam location relative to the electrode. Also, the A-K gap closure leads to an increase in electric field strength in the gap which enhances the particle emission from the electrode surfaces, further contributing to a higher measured than modeled areal density measurement.

5.4.3. Hardware Set #2

Hardware set #2 represents the larger 3.00×2.00 mm cathode and 1.70 mm gap spacing. The areal density measurement collected on Mykonos shots #015624 and #015630 were obtained while probing in the middle of the A-K gap, shown in Fig. (5.22a).

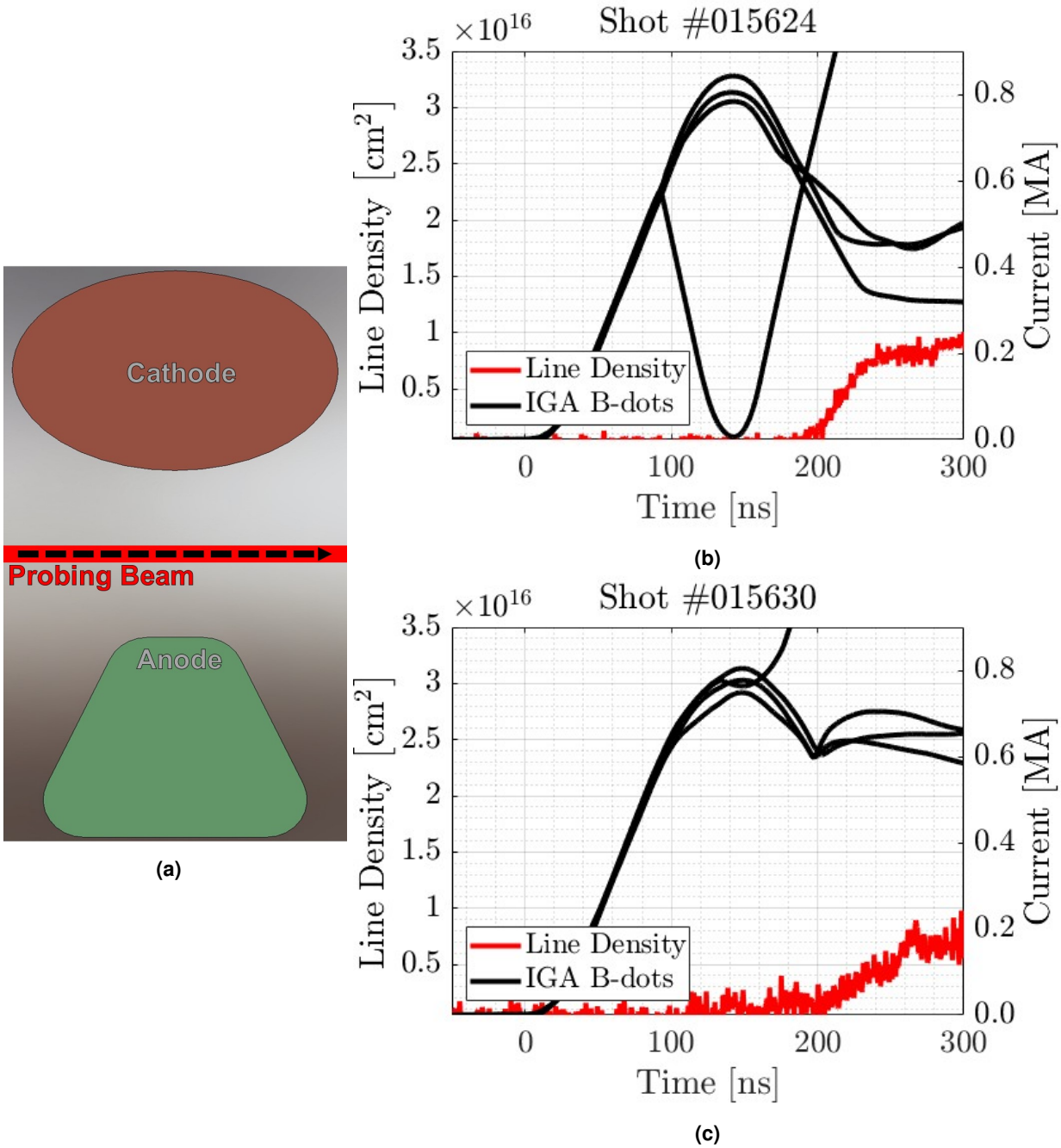

Figure 5.22. On the left is (a) the axial view of A-K hardware set #2 with the representative SHOP interferometer probing beam size and location used to collect data during (b) shot #015624 and (c) shot #015630.

Compared to the colinear SHOP interferometer's areal density measurement on hardware set #1, the plasma measurement made on the hardware set #2 A-K geometry and probing location is significantly delayed and reduced. This could be caused by any of, or a combination of, several factors:

(1) The larger cathode size significantly reduced the current density and thus significantly delayed Joule heating. This could delay the ion/neutral emission and reduce the number of monolayers allowed to desorb.

(2) The increased A-K gap spacing reduced the inner gap electric field strength, leading to less charged particle stripping from the electrodes and less particle bombardment heating on the electrodes.

(3) The larger cathode experiences less hydrodynamic gap closure, leading to lower electric field strengths and less particle emission enhancement effects.

(4) Or, simply probing in the middle of the gap is a significant enough variation compared to probing close to the cathode surface to justify the delay and reduction in plasma areal density measured.

CHICAGO simulation heat map images highlighting the electron density spatial variation for hardware set #2 are shown in Fig. (5.23).

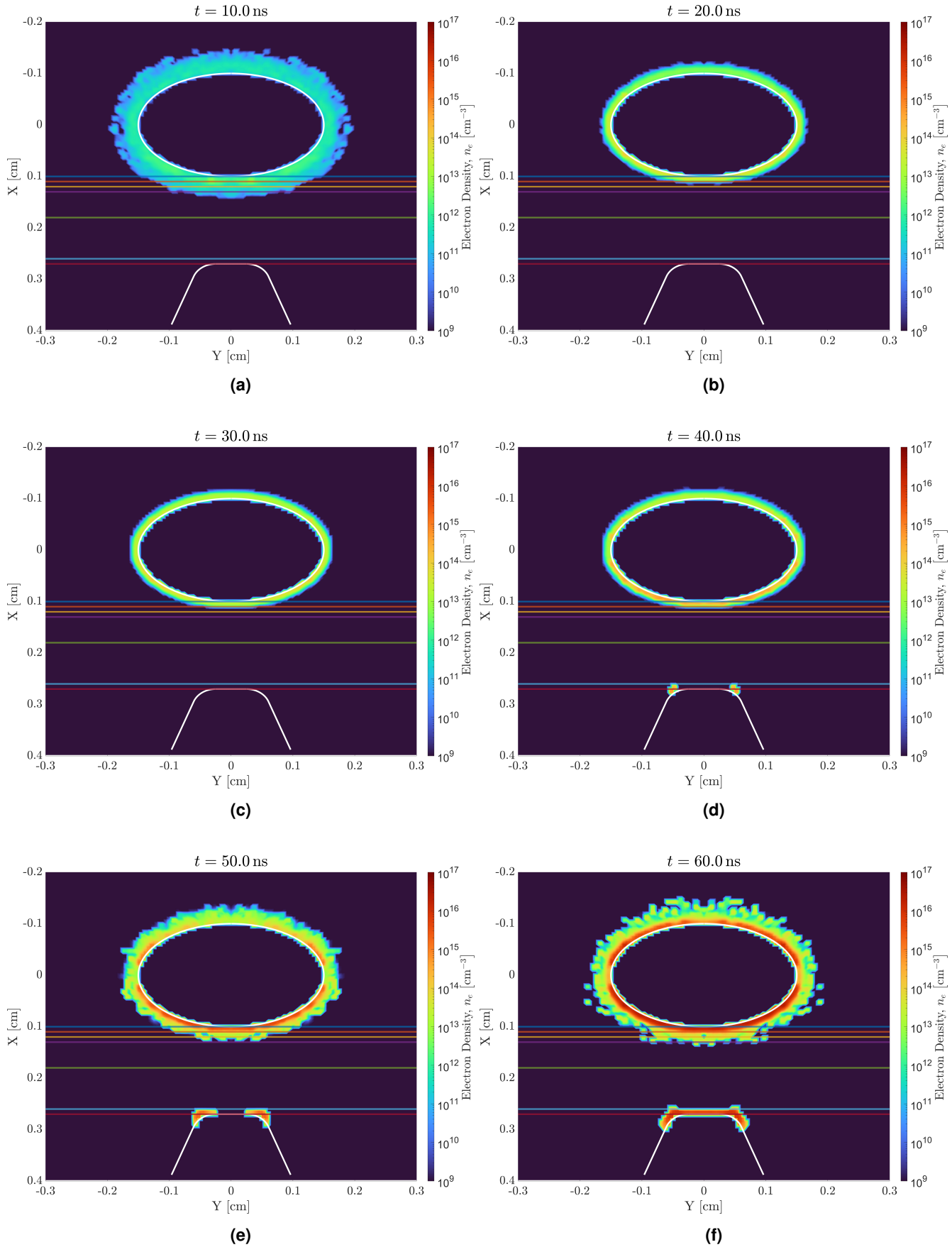

Figure 5.23. Several heat map images showing the CHICAGO simulation's spatially resolved electron densities [cm^{-3}] of the 3.00×2.00 mm cathode with a 1.70 mm gap spacing hardware geometry. Shown are images corresponding to time stamps of (a) 10 ns, (b) 20 ns, (c) 30 ns, (d) 40 ns, (e) 50 ns, and (f) 60 ns during the Mykonos current pulse.

Various temporal lineout x areal density calculations from the 3.00×2.00 mm cathode with a 1.70 mm gap spacing hardware geometry CHICAGO simulation are shown in Fig. (5.24). The variable weight macro particles on the edge surface between vacuum and plasma lead to statistical noise, so a 2 ns (20 point) moving average was taken.

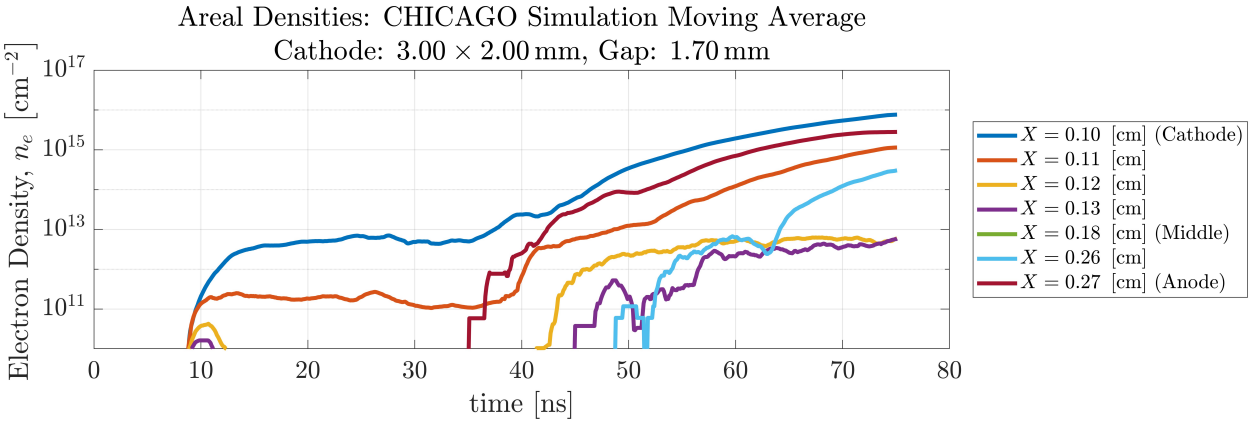

Figure 5.24. 2 ns moving averages of the various temporal x lineout areal density calculations from the 3.00×2.00 mm cathode with a 1.70 mm gap spacing hardware geometry CHICAGO simulation.

The CHICAGO simulation for hardware set #2 in ongoing, but as of now it has reached 75.1 ns. The $x = 0.18$ cm (middle of the A-K gap) CHICAGO lineout result never exceeds 10^{10} cm^{-2} in the first 75.1 ns of the simulation, so it is not worth plotting the colinear SHOP interferometer in the same figure as the CHICAGO lineouts. The colinear SHOP interferometer did not detect any areal densities above its sensitivity limit of 1×10^{15} in the first 75 ns, corroborating the CHICAGO results to some extent.

The 100 μm away from cathode lineout for hardware set #1 exceeded 10^{14} cm^{-2} at 55 ns, but the 100 μm away from cathode lineout for hardware set #2 exceeded 10^{14} cm^{-2} at 59 ns. This agrees with the first above mentioned possibility for the experimental areal density delay, the delay is partially due to the geometry not solely probing location. Though 4 ns delay in 10^{14} cm^{-2} plasmas close to the cathode may seem insignificant, it may translate to a substantial delay in the 10^{15} cm^{-2} plasmas formation in the middle of the gap.

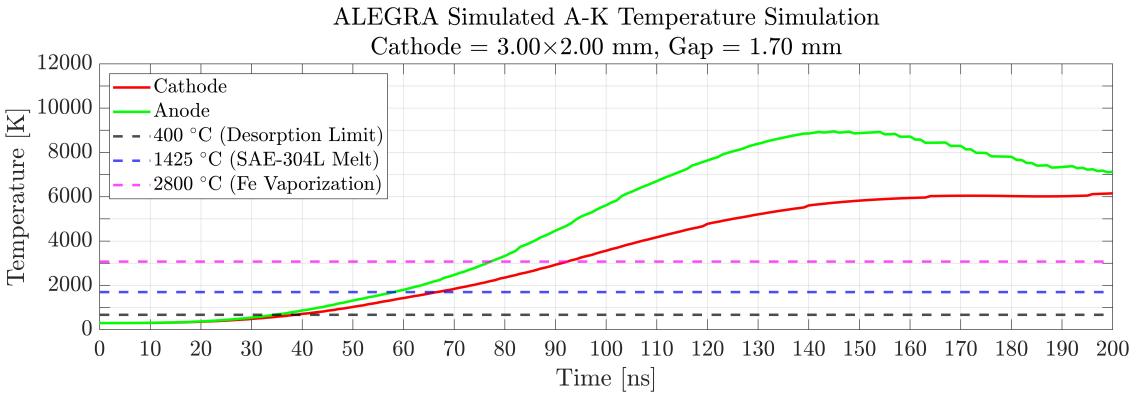

Figure 5.25. ALEGRA simulation results for the anode and cathode surface temperatures along the center line (where the A-K gap spacing is smallest).

The simulation results in Fig. (5.25) suggests the electrodes exceed the 400°C desorption threshold at 39 ns and 35 ns for the cathode and anode respectively, matching the above Fig. (5.24) CHICAGO lineouts transition from decreasing areal density to increasing at 35 ns. Also, the cathode and anode each exceed the melt temperature of SAE-304L at 67 ns and 58 ns respectively.

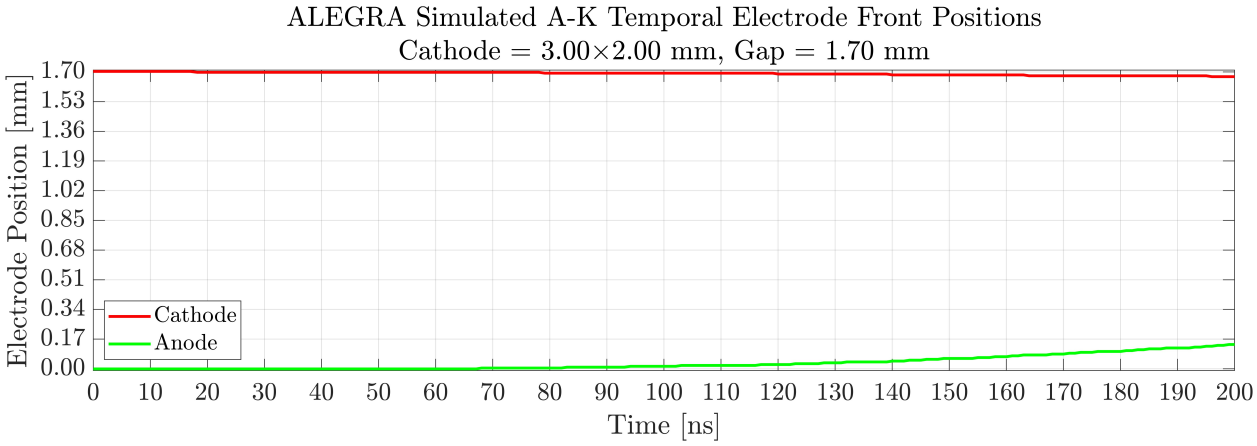

Figure 5.26. ALEGRA simulation results for the anode and cathode surface fronts along the center line (where the A-K gap spacing is smallest). This shows the high density material moving inward and reducing the gap spacing.

The simulation results shown in Fig. (5.26) highlight significantly less gap closure occurring in the hardware set #2 geometry than the hardware set #1 geometry shown in Fig. (5.21). This would imply more accurate CHICAGO simulations and justify less colinear SHOP interferometer probe beam blocking when probing close to the electrodes.

6. CONCLUSION

The conclusionary chapter will summarize the work completed throughout the LDRD and provide a description of it's impact on power flow research. There is also a section comparing the developed colinear SHOP interferometer's capabilities to that of the previously fielded Photonic Doppler Velocimetry (PDV) interferometer. It finishes with a short discussion on future work.

6.1. Summary

Motivated by the need for accurate measurment of low density MITL plasmas, this LDRD supported the development and commissioning of a new optical interferometer. To measure the expected 10^{13} - $10^{17}\,\mathrm{cm}^{-3}$ electron densities inside the 0.5 - 6 mm Anode-Cathode (A-K) gaps, a colinear SHOP interferometer diagnostic was constructed. The diagnostic was initially fielded on the University of New Mexico (UNM) Helicon-Cathode (HelCat) plasma device. This device provided a highly repeatable and well understood plasma source for which the colinear SHOP interferometer's functionality could be verified and measured. The work at UNM lead to the publication of a Review of Scientific Instruments (RSI) publication [20], DOI:10.1063/5.0101687.

After the diagnostic's capability was proven at UNM, the colinear SHOP interferometer was commissioned for use on the Sandia National Laboratories (SNL) Mykonos accelerator. Here, it provided the first direct temporally resolved areal density measurements of plasma formation in a parallel plate MITL. The diagnostic was able to achieve an areal density sensitivity of $1 \times 10^{15}\,\mathrm{cm}^{-2}$ along a $\sim 2\,\mathrm{mm}$ probing path length, which provided new data on MITL plasma formation. In conjunction, CHICAGO three-dimensional fully electromagnetic Particle-In-Cell (PIC) and ALEGRA shock hydrodynamics and multiphysics model simulations were conducted for the same parallel plate geometry and both simulations support the diagnostics experimental findings. More computational and experimental work will continue on this parallel plate geometry, likely leading to another publication(s). The smaller scale Mykonos accelerator work has also provided justification that the colinear SHOP interferometer is a capable diagnostic for measuring plasma areal densities in the inner MITL and convolute regions of larger TW-class accelerators like SNL's *Z* machine. However, as discussed below, the presently designed colinear SHOP interferometer may not be the best diagnostic option for such a measurement on *Z*.

6.2. Comparison to PDV Diagnostic

An experimental diagnostic meeting almost all the criteria mentioned in Sec. (1.1), has been fielded for PF research to measure the A-K gap plasma electron areal density (or more accurately,

refractive index) near a liner pinch load on the Z machine. The diagnostic was a fiber-based Photonic Doppler Velocimetry (PDV) interferometer [41], [42].The PDV diagnostic measures "apparent velocities" $v^*(t)$, which result from time varying changes in the refractive index $\widetilde{n}$ along the probing path length L via

$$v^*(t) = -\frac{d}{dt}\int_0^L \widetilde{n}(x,t)\,dx. \tag{6.1}$$

Both the PDV and colinear SHOP interferometer diagnostics are line-averaged ("areal") refractive index measurements. Therefore, along the probing beam's path there can be no distinction made between a uniform density plasma vs. one with high density gradients. The PDV diagnostic probed the inner MITL plasma with a $\lambda = 1550\,\text{nm}$, $500\,\mu\text{m}$ diameter beam along a $20\,\text{mm}$ path length. Since the PDV diagnostic utilizes an unpolarized single wavelength probing beam (compared to the two-color linearly polarized approach of the colinear SHOP interferometer), the wave can be easily fiber coupled for long distances, increasing it's ability to access the difficult geometry of the inner MITL.

In addition, the PDV diagnostic achieved a minimum resolvable refractive index sensitivity of $\widetilde{n} = 1\times10^{-7}$, as well as a bandwidth limited maximum resolvable refractive index change of $\Delta\widetilde{n} = 1\times10^{-3}\,\text{ns}^{-1}$. These sensitivities correspond to a capability to make electron areal density measurements above $\langle n_e L\rangle > 1.8\times10^{14}\,\text{cm}^{-2}$ and less than $\Delta\langle n_e L\rangle < 1.8\times10^{18}\,\text{cm}^{-2}\,\text{ns}^{-1}$. Considering the benefits listed above, our conclusion is that the PDV diagnostic utilized in [41], [42] is presently a more capable diagnostic for low areal density inner MITL plasma measurements than the presented colinear SHOP interferometer diagnostic.

However, a drawback to the PDV diagnostic is that integration drift can lead to false index change measurements and there is a trade-off between density sensitivity and temporal resolution. Additionally, the PDV optical system is not inherently isolated to mechanical vibrations like the colinear SHOP interferometer. Future advancements to the SHOP interferometer may allow for similar sensitivity capabilities to the PDV interferometer and will therefore be the focus of future work, as discussed in Sec. (6.3). There is a path forward for the colinear SHOP interferometer to continue to be improved and to eventually fill a diagnostic role for areal density measurements in the inner MITL and convolute regions of larger TW-class accelerators like SNL's Z machine.

6.3. Future Work

The colinear SHOP interferometer's present sensitivity limit of $1\times10^{15}\,\text{cm}^{-2}$ is adequate enough to conduct new fundamental physics experiments on the Mykonos parallel plate MITL hardware, therefore it will continue to be fielded. However, improvements on the system's detection scheme (like more sensitive detectors) and second-harmonic conversion efficiency (leading to more optical power reaching the detectors) will increase the diagnostic's signal-to-noise ratio, lowering the areal density sensitivity below the present limit. Lowering the diagnostic's sensitivity limit will expand the fundamental physics research possibilities. Until the colinear SHOP interferometer's sensitivity limit is lowered, it is not expected that it will replace the PDV interferometer diagnostic for Z machine inner MITL measurements.

REFERENCES

[1] D. B. Sinars, M. A. Sweeney, C. S. Alexander, *et al.*, "Review of pulsed power-driven high energy density physics research on z at sandia," *Physics of Plasmas*, vol. 27, no. 7, 2020, ISSN: 1070-664X. DOI: 10.1063/5.0007476. [Online]. Available: https://doi.org/10.1063/5.0007476.

[2] D. V. Rose, D. R. Welch, C. L. Miller, *et al.*, "10^7-a load-current *B*-dot monitor: Simulations, design, and performance," *Physical Review Special Topics - Accelerators and Beams*, vol. 13, no. 4, p. 040 401, 2010, PRSTAB. DOI: 10.1103/PhysRevSTAB.13.040401. [Online]. Available: https://link.aps.org/doi/10.1103/PhysRevSTAB.13.040401.

[3] M. R. Gomez, R. M. Gilgenbach, M. E. Cuneo, *et al.*, "Experimental study of current loss and plasma formation in the *Z* machine post-hole convolute," *Physical Review Accelerators and Beams*, vol. 20, no. 1, p. 010 401, 2017, PRAB. DOI: 10.1103/PhysRevAccelBeams.20.010401. [Online]. Available: https://link.aps.org/doi/10.1103/PhysRevAccelBeams.20.010401.

[4] G. R. Laity, C. Aragon, N. L. Bennett, *et al.*, "Recent diagnostic platform accomplishments for studying vacuum power flow physics at the sandia z accelerator," Sandia National Lab.(SNL-NM), Albuquerque, NM (United States); Sandia . . ., Report, 2018.

[5] M. R. Gomez, S. A. Slutz, C. A. Jennings, *et al.*, "Performance scaling in magnetized liner inertial fusion experiments," *Physical Review Letters*, vol. 125, no. 15, p. 155 002, 2020, PRL. DOI: 10.1103/PhysRevLett.125.155002. [Online]. Available: https://link.aps.org/doi/10.1103/PhysRevLett.125.155002.

[6] D. V. Rose, E. A. Madrid, D. R. Welch, *et al.*, "Computational analysis of current-loss mechanisms in a post-hole convolute driven by magnetically insulated transmission lines," *Physical Review Special Topics - Accelerators and Beams*, vol. 18, no. 3, p. 030 402, 2015, PRSTAB. DOI: 10.1103/PhysRevSTAB.18.030402. [Online]. Available: https://link.aps.org/doi/10.1103/PhysRevSTAB.18.030402.

[7] N. Bennett, D. Welch, C. Jennings, *et al.*, "Current transport and loss mechanisms in the z accelerator," *Physical Review Accelerators and Beams*, vol. 22, no. 12, p. 120 401, 2019.

[8] N. Bennett, D. R. Welch, G. Laity, D. V. Rose, and M. E. Cuneo, "Magnetized particle transport in multi-ma accelerators," *Physical Review Accelerators and Beams*, vol. 24, no. 6, p. 060 401, 2021, PRAB. DOI: 10.1103/PhysRevAccelBeams.24.060401. [Online]. Available: https://link.aps.org/doi/10.1103/PhysRevAccelBeams.24.060401.

[9] N. Bennett, D. R. Welch, K. Cochrane, *et al.*, "Electrode plasma formation and melt in z-pinch accelerators," *Physical Review Accelerators and Beams*, vol. 26, no. 4, p. 040 401, 2023, PRAB. DOI: 10.1103/PhysRevAccelBeams.26.040401. [Online]. Available: https://link.aps.org/doi/10.1103/PhysRevAccelBeams.26.040401.

[10] W. A. Stygar, P. A. Corcoran, H. C. Ives, *et al.*, "55-tw magnetically insulated transmission-line system: Design, simulations, and performance," *Physical Review Special Topics - Accelerators and Beams*, vol. 12, no. 12, p. 120 401, 2009, PRSTAB. DOI: 10.1103/PhysRevSTAB.12.120401. [Online]. Available: https://link.aps.org/doi/10.1103/PhysRevSTAB.12.120401.

[11] D. R. Baker and S.-T. Lee, "Dual laser interferometer for plasma density measurements on large tokamaks," *Review of Scientific Instruments*, vol. 49, no. 7, pp. 919–922, 1978, ISSN: 0034-6748. DOI: 10.1063/1.1135492. [Online]. Available: https://doi.org/10.1063/1.1135492.

[12] F. A. Hopf, A. Tomita, and G. Al-Jumaily, "Second-harmonic interferometers," *Optics Letters*, vol. 5, no. 9, pp. 386–388, 1980. DOI: 10.1364/OL.5.000386. [Online]. Available: https://opg.optica.org/ol/abstract.cfm?URI=ol-5-9-386.

[13] F. A. Hopf, A. Tomita, G. Al-Jumaily, M. Cervantes, and T. Liepmann, "Second-harmonic interferometers ii," *Optics Communications*, vol. 36, no. 6, pp. 487–490, 1981, ISSN: 0030-4018. DOI: https://doi.org/10.1016/0030-4018(81)90199-1. [Online]. Available: https://www.sciencedirect.com/science/article/pii/0030401881901991.

[14] F. A. Hopf and M. Cervantes, "Nonlinear optical interferometer," *Applied Optics*, vol. 21, no. 4, pp. 668–677, 1982. DOI: 10.1364/AO.21.000668. [Online]. Available: https://opg.optica.org/ao/abstract.cfm?URI=ao-21-4-668.

[15] V. P. Drachev, Y. I. Krasnikov, and P. A. Bagryansky, "Dispersion interferometer for controlled fusion devices," *Review of Scientific Instruments*, vol. 64, no. 4, pp. 1010–1013, 1993, ISSN: 0034-6748. DOI: 10.1063/1.1144170. [Online]. Available: https://doi.org/10.1063/1.1144170.

[16] V. Licht and H. Bluhm, "A sensitive dispersion interferometer with high temporal resolution for electron density measurements," *Review of Scientific Instruments*, vol. 71, no. 7, pp. 2710–2715, 2000, ISSN: 0034-6748. DOI: 10.1063/1.1150679. [Online]. Available: https://doi.org/10.1063/1.1150679.

[17] F. Brandi and F. Giammanco, "Versatile second-harmonic interferometer with high temporal resolution and high sensitivity based on a continuous-wave nd:yag laser," *Optics Letters*, vol. 32, no. 16, pp. 2327–2329, 2007. DOI: 10.1364/OL.32.002327. [Online]. Available: https://opg.optica.org/ol/abstract.cfm?URI=ol-32-16-2327.

[18] F. Brandi, F. Giammanco, W. S. Harris, T. Roche, E. Trask, and F. J. Wessel, "Electron density measurements of a field-reversed configuration plasma using a novel compact ultrastable second-harmonic interferometer," *Review of Scientific Instruments*, vol. 80, no. 11, 2009, ISSN: 0034-6748. DOI: 10.1063/1.3258199. [Online]. Available: https://doi.org/10.1063/1.3258199.

[19] F. Brandi, F. Wessel, C. M. Lohff, J. R. Duff, and Z. O. Haralson, "Experimental study on the performances of second-harmonic dispersion interferometers at 10.6 μm and 1064 nm for plasma density measurements," *Applied Optics*, vol. 59, no. 27, pp. 8486–8493, 2020. DOI: 10.1364/AO.399551. [Online]. Available: https://opg.optica.org/ao/abstract.cfm?URI=ao-59-27-8486.

[20] N. R. Hines, S. Patel, D. Scoglietti, *et al.*, "A fiber-coupled dispersion interferometer for density measurements of pulsed power transmission line electron sheaths on sandia's z machine," *Review of Scientific Instruments*, vol. 93, no. 11, p. 113 505, 2022. DOI: 10.1063/5.0101687. [Online]. Available: https://aip.scitation.org/doi/abs/10.1063/5.0101687.

[21] F. C. Jobes and N. L. Bretz, "A prototype imaging second harmonic interferometer," *Review of Scientific Instruments*, vol. 68, no. 1, pp. 709–712, 1997, ISSN: 0034-6748. DOI: 10.1063/1.1147681. [Online]. Available: https://doi.org/10.1063/1.1147681.

[22] F. Brandi and F. Wessel, "Widefield quantitative phase imaging by second-harmonic dispersion interferometry," *Optics Letters*, vol. 45, no. 15, pp. 4304–4307, 2020. DOI: 10.1364/OL.395097. [Online]. Available: https://opg.optica.org/ol/abstract.cfm?URI=ol-45-15-4304.

[23] C. T. Chavez, A. Egly, I. Sepulveda, and F. J. Wessel, "Measurement of 2d density profiles using a second-harmonic, dispersion interferometer," *Review of Scientific Instruments*, vol. 94, no. 2, 2023, ISSN: 0034-6748. DOI: 10.1063/5.0119896. [Online]. Available: https://doi.org/10.1063/5.0119896.

[24] K. L. Jensen, *Introduction to the physics of electron emission*. John Wiley and Sons, 2018, ISBN: 1119051894.

[25] I. Langmuir, "The effect of space charge and residual gases on thermionic currents in high vacuum," *Physical Review*, vol. 2, no. 6, pp. 450–486, 1913, PR. DOI: 10.1103/PhysRev.2.450. [Online]. Available: https://link.aps.org/doi/10.1103/PhysRev.2.450.

[26] T. W. L. Sanford, J. A. Halbleib, J. W. Poukey, *et al.*, "Measurement of electron energy deposition necessary to form an anode plasma in ta, ti, and c for coaxial bremsstrahlung diodes," *Journal of Applied Physics*, vol. 66, no. 1, pp. 10–22, 1989, ISSN: 0021-8979. DOI: 10.1063/1.343913. [Online]. Available: https://doi.org/10.1063/1.343913.

[27] M. E. Cuneo, P. R. Menge, D. L. Hanson, *et al.*, "Results of vacuum cleaning techniques on the performance of lif field-threshold ion sources on extraction applied-b ion diodes at 1-10 tw," *IEEE transactions on plasma science*, vol. 25, no. 2, pp. 229–251, 1997, ISSN: 0093-3813.

[28] M. E. Cuneo, "The effect of electrode contamination, cleaning and conditioning on high-energy pulsed-power device performance," *IEEE transactions on dielectrics and electrical insulation*, vol. 6, no. 4, pp. 469–485, 1999, ISSN: 1070-9878.

[29] W. A. Stygar, S. E. Rosenthal, H. C. Ives, *et al.*, "Energy loss to conductors operated at lineal current densities $\leq 10\ MA/cm$: Semianalytic model, magnetohydrodynamic simulations, and experiment," *Physical Review Special Topics - Accelerators and Beams*, vol. 11, no. 12, p. 120 401, 2008, PRSTAB. DOI: 10.1103/PhysRevSTAB.11.120401. [Online]. Available: https://link.aps.org/doi/10.1103/PhysRevSTAB.11.120401.

[30] E. M. Waisman, M. Desjarlais, and M. Cuneo, "Ion current losses in the convolute and inner magnetically insulated transmission line of the z machine," *Physical Review Accelerators and Beams*, vol. 22, no. 3, p. 030 402, 2019.

[31] A. C. La Fontaine, "Ion emission at the target of the radiographic devices pivair and airix," *Journal of Physics D: Applied Physics*, vol. 40, no. 6, p. 1712, 2007, ISSN: 0022-3727.

[32] *Cefl-kilo continuous wave erbium fiber laser*, Web Page. [Online]. Available: http://www.keopsys.com/wp-content/uploads/PDF/CEFL-KILO_brochure-v1-0.pdf.

[33] *Shg standard chips*, Web Page. [Online]. Available: https://www.hcphotonics.com/portfolio/items/shg.

[34] *Compact oven for nonlinear crystals – heatpoint*, Web Page. [Online]. Available: https://eksmaoptics.com/out/media/EKSMA_Optics_Compact_Oven_for_Nonlinear_Crystals-Heatpoint.pdf.

[35] A. G. Lynn, M. Gilmore, C. Watts, *et al.*, "The helcat dual-source plasma device," *Review of Scientific Instruments*, vol. 80, no. 10, 2009, ISSN: 0034-6748.

[36] M. G. Mazarakis, W. E. Fowler, K. LeChien, *et al.*, "High-current linear transformer driver development at sandia national laboratories," *IEEE transactions on plasma science*, vol. 38, no. 4, pp. 704–713, 2010, ISSN: 0093-3813.

[37] D. C. Lamppa, J. P. VanDevender, B. T. Hutsel, *et al.*, "Diagnosing z machine current loss using anode-side charged particle diagnostics," Sandia National Lab.(SNL-NM), Albuquerque, NM (United States), Report, 2017.

[38] D. Lamppa, S. Simpson, B. Hutsel, M. Cuneo, G. Laity, and D. Rose, "Assessment of electrode contamination mitigation at 0.5 ma scale," Sandia National Lab.(SNL-NM), Albuquerque, NM (United States), Report, 2021.

[39] D. Lamppa, D. Rose, B. Hutsel, G. Laity, and M. Cuneo, "Assessing the effect of in-situ plasma cleaning on electrode plasma formation in a 650-ka mitl," in *2022 IEEE International Conference on Plasma Science (ICOPS)*, IEEE, pp. 1–1, ISBN: 1665479256.

[40] J. Chen, "Shadowgraphy and schlieren images of mykonos plasma formation ak gap hardware," The University of Michigan, Report, 2022, Unpublished.

[41] D. Dolan, K. Bell, B. Fox, *et al.*, "Plasma and radiation detection via fiber interferometry," *Journal of Applied Physics*, vol. 123, no. 3, p. 034 502, 2018, ISSN: 0021-8979.

[42] A. Porwitzky, D. H. Dolan, M. R. Martin, G. Laity, R. W. Lemke, and T. R. Mattsson, "Direct measurements of anode/cathode gap plasma in cylindrically imploding loads on the z machine," *Physics of Plasmas*, vol. 25, no. 6, 2018, ISSN: 1070-664X. DOI: 10.1063/1.5026225. [Online]. Available: https://doi.org/10.1063/1.5026225.

DISTRIBUTION

Email—Internal

Name	Org.	Sandia Email Address
Nathan R. Hines	1659	nhines@sandia.gov
Thomas J. Awe	1681	tjawe@sandia.gov
Jens Schwarz	1659	jschwar@sandia.gov
Sonal G. Patel	6772	spatel@sandia.gov
Derek C. Lamppa	1659	dclampp@sandia.gov
Pablo A. Reyes	1659	pareyes@sandia.gov
Daniel J. Scoglietti	1659	djscogl@sandia.gov
Darrell J. Armstrong	1682	darmstr@sandia.gov
David E. Bliss	1659	debliss@sandia.gov
Michael E. Cuneo	1650	mecuneo@sandia.gov
Technical Library	1911	sanddocs@sandia.gov

Email—External

Name	Company Email Address	Company Name
Nathan R. Hines	nathan191@unm.edu	The University of New Mexico
David V. Rose	davidr@vosssci.com	Voss Scientific
Mark A. Gilmore	mgilmore@unm.edu	The University of New Mexico
George R. Laity	grlaity@lanl.gov	Los Alamos National Laboratory (LANL)

Hardcopy—Internal

Number of Copies	Name	Org.	Mailstop
1	Nathan R. Hines	1659	1195
1	L. Martin, LDRD Office	1910	0359

Sandia National Laboratories

Sandia National Laboratories is a multimission laboratory managed and operated by National Technology & Engineering Solutions of Sandia LLC, a wholly owned subsidiary of Honeywell International Inc., for the U.S. Department of Energy's National Nuclear Security Administration under contract DE-NA0003525.